

OPTICAL MASS FLOW DIAGNOSTICS IN HERBIG AE/BE STARS

P. WILSON CAULEY¹

Wesleyan University and
Department of Astronomy and Van Vleck Observatory, 96 Foss Hill Dr., Middletown, CT 06459

CHRISTOPHER M. JOHNS–KRULL¹

Rice University and
Department of Physics and Astronomy, 6100 Main St., MS 108, Houston, TX 77005

ACCEPTED TO APJ: June 24, 2015

ABSTRACT

We examine a broad range of mass flow diagnostics in a large sample of Herbig Ae/Be stars (HAEBES) using high resolution optical spectra. The H β and He I 5876 Å lines show the highest incidence of P–Cygni (30%) and inverse P–Cygni (14%) morphologies, respectively. The Fe II 4924 Å line also shows a large incidence of P–Cygni profiles (11%). We find support for many of the conclusions reached in a study based on the analysis of the He I λ 10830 line in a large sample of HAEBES. Namely, HAEBES exhibit smaller fractions of both blue–shifted absorption (i.e. mass outflow) and red–shifted absorption (i.e. mass infall or accretion) than their lower mass cousins, the classical T Tauri stars (CTTSs). In particular, the optical data supports the conclusion that HAEBES displaying red–shifted absorption, in general, show maximum red–shifted absorption velocities that are smaller fractions of their stellar escape velocities than is found for CTTSs. This suggests that HAEBE accretion flows are originating deeper in the gravitational potentials of their stars than in CTTS systems. In addition, we find a lack of inner disk wind signatures in the blue–shifted absorption objects; only stellar wind signatures are clearly observed. These findings, along with the lack of detected magnetic fields around HAEBES, support the idea that large magnetospheres are not prevalent around HAEBES and that accretion flows are instead mediated by significantly smaller magnetospheres with relatively smaller truncation radii (e.g. 1–2 R_*). Red–shifted absorption is much more common around Herbig Ae stars than Be stars, suggesting that Herbig Be stars may accrete via a boundary layer rather than along magnetic field lines.

Subject headings: accretion–stars:pre–main sequence–stars:variables:T Tauri, Herbig Ae/Be–stars:winds,outflows–methods:statistical

1. INTRODUCTION

The interplay between mass loss and accretion in pre–main sequence systems is important in determining both the final stellar mass, the mass in the disk available to form planets, and the local physical conditions (e.g. incident UV flux, temperature) affecting planet formation and evolution. While many details of the physical mechanisms involved in mass accretion and mass outflow in the immediate circumstellar environments ($r \lesssim 0.1$ AU) for low–mass Class II pre–main sequence stars, or classical T Tauri stars (CTTSs), are now understood (e.g. Muzerolle et al. 2001; Romanova et al. 2009), the picture is less clear concerning these processes around the intermediate mass Herbig Ae/Be stars (HAEBES).

Optical spectroscopic investigations into the nature of the circumstellar environments around HAEBES have been numerous. A small number of these studies have been performed on medium or large samples of HAEBES. Finkenzeller & Mundt (1984) presented medium resolution ($\Delta v \sim 16$ km s^{−1}) H α and Na I D lines for a sample of 43 HAEBES that focused mainly on the P–Cygni

profiles of a small number (8) of objects. The investigations of Hamann & Persson (1992), Böhm & Catala (1994), and Böhm & Catala (1995) all examined samples of ~ 30 HAEBES and a small or medium number of spectral line diagnostics. Hamann & Persson (1992) and Böhm & Catala (1994) compare their samples to known TTS characteristics but these studies focus mainly on pure emission line morphologies and not on red and blue–shifted absorption. Vieira et al. (2003), in a spectroscopic HAEBE study covering the largest number of objects to date, classified the H α profiles of 131 stars using low and medium resolution spectra. Vieira et al. (2003) also examined forbidden line emission in their sample. However, no detailed interpretation of the H α profile morphologies or forbidden line strengths are performed, yielding little information about the kinematics of the inner circumstellar material. Finally, the HAEBE variability study of Mendigutía et al. (2011) examined H α , [O I]6300, He I 5876, and the Na I D lines in a medium sized sample using medium resolution spectra. High spectral resolution observations of a wide range of accretion and outflow diagnostics in a large sample of HAEBES is clearly needed.

Besides the studies listed above, most optical spectroscopic HAEBE studies have focused on single objects or small sample sizes and a small number of spectral line diagnostics (e.g. Catala et al. 1993; Kraus et al. 2008;

pcauley@wesleyan.edu
cmj@rice.edu

¹ Visiting Astronomer, McDonald Observatory, The University of Texas, Austin, TX 78712, USA

Grady et al. 2010). While this is useful for providing details about specific objects, studies of this sort provide little information concerning the physical characteristics of mass flows around HAEBES as a group, which are important for illuminating the general differences between the early evolution of low and intermediate mass pre-main sequence stars. Comparing large sample of HAEBES and CTTs can also provide insight into the important physical mechanisms responsible for generating mass flows in young stars.

While both HAEBES and CTTs host gaseous accretion disks, the lack of strong detected magnetic fields on HAEBES (e.g. Wade et al. 2007; Alecian et al. 2013) and their large $v_{\text{sin}i}$ values compared to CTTs Johns-Krull (2007) provide hints that accretion and outflow processes do not proceed identically in both groups of objects. Magnetospheric accretion, widely accepted to operate in most CTT systems, funnels material from a truncated inner disk onto the surface of the star (Königl 1991). Accretion along magnetic field lines is not possible from outside of a narrow region around the corotation radius in the disk (Shu et al. 1994). Muzerolle et al. (2004) pointed out that in order for magnetospheric accretion to operate around HAEBES, the large $v_{\text{sin}i}$ values of HAEBES require the corotation radii, and thus the magnetic truncation radii, to be closer to the stellar surface than in CTTs. This has implications for the ability of HAEBES to launch accretion-generated outflows in the same way as CTTs (see §of Cauley & Johns-Krull 2014, for an expanded discussion). Spectral line profile morphologies can provide insight into how these mass flows are generated.

In this paper we present a high resolution optical study of a large sample of HAEBES using a large number of spectral line diagnostics with the goal of investigating differences in the accretion and outflow mechanisms operating around HAEBES compared to CTTs. This work is the second part of a multi-wavelength study of accretion and outflows in HAEBES. The first part is presented in Cauley & Johns-Krull (2014, hereafter Paper I), and focused on the study of He I $\lambda 10830$ in a sample of 56 HAEBES. Our comprehensive coverage of optical

mass flow indicators enables us to derive reliable estimates and confidence intervals of the incidence of accretion and outflow signatures in HAEBES. We describe our observations and data reduction in §2. In §3 we discuss the calculation of stellar radial velocities and rotational velocities. Section 4 covers the classification of the line profiles. We present the individual line and overall mass flow statistics in §5, as well as a comparison to the He I $\lambda 10830$ statistics from Paper I. A comparison of the entire sample statistics to those of CTTs is also given in §5. Section 6 investigates the physical cause of the differences in morphology statistics. Our conclusions are summarized in §7.

2. OBSERVATIONS AND DATA REDUCTION

Our sample consists of 87 HAEBES covering a wide range of spectral types and was chosen from the catalogues of Vieira et al. (2003); Thé, de Winter, & Pérez (1994); and Finkenzeller & Mundt (1984). Classification as a HAEBE in a previous survey was the only selection criteria. It is important to note that our sample likely contains objects at various phases in their pre-main sequence evolution. However, the small number of HAEBES currently identified in the literature weakens the significance of a more specific comparison between distinct evolutionary groups. Thus we include all objects in our central analysis regardless of spectral type and estimated age, though presumably all are pre-main sequence in nature.

2.1. Observations

Our observations were performed using two cross-dispersed echelle spectrographs on two telescopes: the Sandiford Echelle Spectrometer (SES McCarthy et al. 1993) on the McDonald Observatory 2.1 m Otto Struve telescope and the Tull 2dCoudé echelle spectrometer (TS2 Tull et al. 1995) on the 2.7 m Harlan J. Smith telescope. The specifics of each observation are given in Table 1. Some objects were observed multiple times during different observing runs. The use of observations from different epochs in the analysis is described in section 5.

Table 1
Log of echelle observations

Object ID (1)	Instrument (2)	Telescope (3)	UT Date (4)	Integration time (s) (5)	S/N @ 6400 Å ^a (6)
AB Aur	TS2	2.7 m	18-Sep-2011	120	65
AE Lep	SES	2.1 m	01-Nov-2012	2400	35
BD+61 154	TS2	2.7 m	20-Sep-2011	2500	45
"	SES	2.1 m	30-Oct-2012	1200	30
"	SES	2.1 m	31-Oct-2012	2000	40
BF Ori	TS2	2.7 m	21-Jan-2013	3000	65
BH Cep	TS2	2.7 m	20-Sep-2011	2500	45
"	SES	2.1 m	01-Nov-2012	3600	30
"	SES	2.1 m	02-Nov-2012	3600	30
CQ Tau	TS2	2.7 m	19-Sep-2011	2100	65
DW CMa	TS2	2.7 m	20-Jan-2013	3600	20
GSC 04794-00827	TS2	2.7 m	21-Jan-2013	3600	50
HD 141569	TS2	2.7 m	20-Sep-2011	180	90
"	TS2	2.7 m	20-Jan-2013	75	60
HD 142666	TS2	2.7 m	20-Jan-2013	600	65
HD 163296	TS2	2.7 m	18-Sep-2011	300	55
HD 169142	TS2	2.7 m	19-Sep-2011	200	50
HD 190073	TS2	2.7 m	18-Sep-2011	180	55
"	TS2	2.7 m	26-Sep-2012	350	60
HD 203024	TS2	2.7 m	20-Sep-2011	390	60

Table 1 — *Continued*

Object ID (1)	Instrument (2)	Telescope (3)	UT Date (4)	Integration time (s) (5)	S/N @ 6400 Å ^a (6)
"	SES	2.1 m	30-Oct-2012	600	30
"	SES	2.1 m	31-Oct-2012	1500	50
HD 244314	TS2	2.7 m	20-Sep-2011	2200	65
"	TS2	2.7 m	20-Jan-2013	3000	80
HD 244604	TS2	2.7 m	20-Sep-2011	1300	75
HD 245185	TS2	2.7 m	19-Sep-2011	2300	65
HD 249879	TS2	2.7 m	26-Sep-2012	3200	60
"	SES	2.1 m	01-Nov-2012	3600	35
"	SES	2.1 m	02-Nov-2012	3600	45
HD 250550	SES	2.1 m	01-Nov-2012	2000	40
"	SES	2.1 m	02-Nov-2012	3000	100
HD 287823	TS2	2.7 m	22-Sep-2011	3000	55
HD 290409	TS2	2.7 m	22-Sep-2011	3000	70
HD 290500	TS2	2.7 m	23-Sep-2011	3600	60
HD 290764	TS2	2.7 m	23-Sep-2011	2400	70
HD 290770	TS2	2.7 m	21-Sep-2011	1200	90
HD 34282	TS2	2.7 m	21-Sep-2011	1500	70
HD 35187	TS2	2.7 m	18-Sep-2011	240	70
"	SES	2.1 m	01-Nov-2012	1200	35
"	SES	2.1 m	02-Nov-2012	2400	40
HD 35929	TS2	2.7 m	18-Sep-2011	400	50
HD 36408	TS2	2.7 m	18-Sep-2011	120	40
HD 37357	TS2	2.7 m	18-Sep-2011	500	55
HD 37411	SES	2.1 m	30-Oct-2012	2400	30
HD 38120	SES	2.1 m	30-Oct-2012	600	30
"	SES	2.1 m	31-Oct-2012	2000	55
HD 50083	TS2	2.7 m	18-Sep-2011	180	50
HK Ori	TS2	2.7 m	21-Sep-2011	3600	30
IL Cep	TS2	2.7 m	20-Sep-2011	1300	80
"	TS2	2.7 m	22-Sep-2011	1200	75
"	TS2	2.7 m	23-Sep-2011	1300	80
IP Per	TS2	2.7 m	19-Sep-2011	2400	70
IRAS 05044-0325	TS2	2.7 m	20-Jan-2013	3200	35
IRAS 06071+2925	TS2	2.7 m	20-Jan-2013	3600	30
IRAS 07061-0414	TS2	2.7 m	21-Jan-2013	3600	60
IRAS 17481-1415	TS2	2.7 m	20-Sep-2011	3600	30
IRAS 18306-0500	TS2	2.7 m	20-Sep-2011	3600	30
IRAS 18454+0250	TS2	2.7 m	19-Sep-2011	3000	20
IRAS 19343+2926	TS2	2.7 m	19-Sep-2011	3000	20
"	TS2	2.7 m	26-Sep-2012	3000	15
"	SES	2.1 m	01-Nov-2012	3600	10
"	SES	2.1 m	02-Nov-2012	3600	10
LkH α 134	TS2	2.7 m	20-Sep-2011	2700	60
"	SES	2.1 m	01-Nov-2012	3600	35
"	SES	2.1 m	02-Nov-2012	3600	40
LkH α 208	SES	2.1 m	01-Nov-2012	3600	35
"	SES	2.1 m	02-Nov-2012	3600	35
"	TS2	2.7 m	22-Jan-2013	3000	65
LkH α 233	TS2	2.7 m	22-Sep-2011	3600	20
"	TS2	2.7 m	26-Sep-2012	3600	20
LkH α 257	TS2	2.7 m	21-Sep-2011	3800	35
LkH α 324	TS2	2.7 m	20-Sep-2011	3600	40
LkH α 339	TS2	2.7 m	22-Jan-2013	1960	20
MWC 1080	TS2	2.7 m	21-Sep-2011	2500	20
"	TS2	2.7 m	22-Sep-2011	2500	20
"	TS2	2.7 m	23-Sep-2011	2500	20
"	SES	2.1 m	30-Oct-2012	2000	20
"	SES	2.1 m	31-Oct-2012	3000	10
MWC 120	TS2	2.7 m	18-Sep-2011	400	80
MWC 137	TS2	2.7 m	20-Jan-2013	1800	15
MWC 147	TS2	2.7 m	26-Sep-2012	600	20
MWC 300	TS2	2.7 m	18-Sep-2011	2700	10
MWC 361	TS2	2.7 m	18-Sep-2011	180	70
MWC 480	TS2	2.7 m	18-Sep-2011	180	50
MWC 610	TS2	2.7 m	18-Sep-2011	360	50
"	TS2	2.7 m	26-Sep-2012	900	60
MWC 614	TS2	2.7 m	18-Sep-2011	120	75
MWC 758	TS2	2.7 m	18-Sep-2011	400	55
MWC 778	SES	2.1 m	30-Oct-2012	3600	10
"	SES	2.1 m	31-Oct-2012	4000	10
MWC 863	TS2	2.7 m	23-Sep-2011	500	50
NZ Ser	TS2	2.7 m	19-Sep-2011	3000	40
R Mon	TS2	2.7 m	26-Sep-2012	2000	20
RR Tau	SES	2.1 m	30-Oct-2012	2500	35
"	SES	2.1 m	31-Oct-2012	3600	35

Table 1 — *Continued*

Object ID (1)	Instrument (2)	Telescope (3)	UT Date (4)	Integration time (s) (5)	S/N @ 6400 Å ^a (6)
"	TS2	2.7 m	20-Jan-2013	3600	55
SV Cep	TS2	2.7 m	20-Sep-2011	2500	65
T Ori	TS2	2.7 m	23-Sep-2011	3000	70
"	SES	2.1 m	30-Oct-2012	1200	20
"	SES	2.2 m	31-Oct-2012	3600	50
UX Ori	TS2	2.7 m	22-Sep-2011	3600	30
UY Ori	SES	2.1 m	30-Oct-2012	3600	20
V1185 Tau	TS2	2.7 m	19-Sep-2011	2400	70
"	SES	2.1 m	30-Oct-2012	2000	30
"	SES	2.1 m	31-Oct-2012	3000	40
V1578 Cyg	TS2	2.7 m	20-Sep-2011	2500	90
"	TS2	2.7 m	22-Sep-2011	2400	90
"	TS2	2.7 m	23-Sep-2011	2400	80
V1685 Cyg	TS2	2.7 m	18-Sep-2011	2500	25
"	TS2	2.7 m	26-Sep-2012	3000	30
"	SES	2.1 m	01-Nov-2012	2000	25
"	SES	2.1 m	02-Nov-2011	3000	30
V1686 Cyg	TS2	2.7 m	19-Sep-2011	3600	20
V1787 Ori	TS2	2.7 m	22-Jan-2013	3600	35
V1818 Ori	TS2	2.7 m	22-Jan-2013	3600	40
V346 Ori	TS2	2.7 m	21-Sep-2011	2400	75
V351 Ori	TS2	2.7 m	18-Sep-2011	650	50
V361 Cep	TS2	2.7 m	18-Sep-2011	2200	50
V373 Cep	TS2	2.7 m	21-Sep-2011	3500	40
V374 Cep	TS2	2.7 m	21-Sep-2011	2800	30
"	TS2	2.7 m	26-Sep-2012	3000	50
"	SES	2.1 m	30-Oct-2012	2000	30
"	SES	2.1 m	31-Oct-2012	2000	60
V380 Ori	SES	2.1 m	30-Oct-2012	2400	15
"	SES	2.1 m	31-Oct-2012	3600	15
V586 Ori	TS2	2.7 m	20-Sep-2011	1500	75
V590 Mon	TS2	2.7 m	21-Jan-2013	3600	40
V599 Ori	TS2	2.7 m	22-Jan-2013	3200	30
V718 Sco	TS2	2.7 m	23-Sep-2011	600	50
V791 Mon	SES	2.1 m	01-Nov-2012	2400	30
"	SES	2.1 m	02-Nov-2012	3600	45
VV Ser	TS2	2.7 m	18-Sep-2011	3000	45
"	TS2	2.7 m	21-Sep-2011	3000	40
"	TS2	2.7 m	22-Sep-2011	3000	40
WW Vul	TS2	2.7 m	18-Sep-2011	1600	40
"	TS2	2.7 m	26-Sep-2012	2000	70
"	SES	2.1 m	30-Oct-2012	600	25
"	SES	2.1 m	31-Oct-2012	1500	45
XY Per	TS2	2.7 m	19-Sep-2011	2000	65
Z CMa	TS2	2.7 m	21-Jan-2013	1800	20

^a Continuum S/N for SES spectra taken on 31-Oct-2012 and 02-Nov-2012 is estimated at 4800 Å.

The TS2 data were obtained during three separate runs in 2011 September (7 nights), 2012 September (3 nights), and 2013 January (3 nights). For the TS2 observations, we employed the 1.2" slit with the E2 grating to achieve a resolving power of $R \sim 60,000$, or a velocity resolution of $\sim 5 \text{ km s}^{-1}$. The grating configuration provided wavelength coverage from approximately 3700–10000 Å. Exposure times were limited to 1-hour in order to maximize the number of objects observed with at least moderate signal-to-noise. A S/N of ~ 50 per pixel is typical for the TS2 data, although this varies from S/N ~ 10 up to ~ 90 depending on a combination of the object brightness and weather conditions during the exposure. ThAr comparison lamp spectra were taken multiple times each night to be used for wavelength calibrations. Flat field exposures were collected at the beginning of each night. Telluric and spectroscopic standards were observed periodically throughout the course of each observing run.

The SES data were collected during a single 4-night

observing run in 2012 October. We used two different grating settings, each one on two separate nights, to record both "red" (5430–6620 Å) and "blue" (4375–4870 Å) wavelengths. This was necessary due to the SES's smaller wavelength coverage (~ 500 –1000 Å) per exposure than that of TS2. Even using two wavelength settings, we were not able to observe all of the spectral diagnostics that are available in the TS2 data. Thus objects that are only observed with the SES are lacking data for some diagnostics. The resolving power for each grating setting is $R \sim 60,000$. ThAr lamp spectra were taken throughout the night and flat field exposures were obtained at the beginning of each night. Telluric and spectroscopic standards were observed, although the spectroscopic standards obtained using the TS2 are used interchangeably due to the almost identical velocity resolutions of the two instruments.

2.2. Data reduction

All observations were reduced using custom IDL routines optimized for extracting echelle spectra. Each object exposure is bias subtracted and divided by a normal-

ized median flat to remove pixel to pixel variations. The spectral orders are located and then fit using a 7th order polynomial. Each order is optimally extracted which also removes most hot pixels and cosmic rays. Wavelength calibrations are performed on the ThAr exposures using a two dimensional polynomial fit to all spectral orders simultaneously. Hundreds of individual lamp lines in the exposures are matched to known atlas wavelengths. This procedure results in dispersion solutions that are accurate to ~ 0.10 pixels, or 0.005 \AA , across the entire spectral range. Telluric absorption was subtracted out of the spectral region near 6300 \AA in order to make identification of the O I $\lambda 6300$ line unambiguous. Due to the prominence of the H α and Na I D lines, telluric absorption in these regions does not affect the classification of the line morphologies since these absorption are small perturbations of the true line profile shape. Equivalent width calculations of H α lines include the telluric features which results in a maximum additional uncertainty of $\sim 0.40 \text{ \AA}$.

Some exposures contain strong telluric O I emission near 5577 , 6300 , and 6363 \AA . We have modified our echelle reduction program to locate the night sky emission above and below the spectral trace of the star and subtract it from the actual object spectrum. However, this routine was not always successful, especially for objects with profiles that were not centered on the slit or for irregularly shaped profiles (e.g. binaries). Thus some profiles contain residual night sky emission (e.g. HD 244314). This extra emission can be identified by its narrow ($\sim 10 \text{ km s}^{-1}$) width and is easily distinguished from the stellar line profile.

Approximate continuum normalization in each order was performed by dividing each order by the blaze function of the same order, derived from the reduced spectrum of the median flat for that particular grating setting. A linear fit is then performed to remove any residual slope. Some objects display strong photospheric Balmer features which have wings that often extend to the ends of the spectral order. The continuum normalization in these cases is likely not exactly the true stellar continuum. However, identification of non-photospheric features in these lines is not problematic with the use of a comparison standard since the chosen continuum level does not affect the line shape. The Fe II 4352 \AA and N II 6583 \AA features often lie on the wings of H γ and H α , respectively. These profiles are normalized to the continuum in the Balmer lines.

3. PHYSICAL PARAMETERS

In order to correctly separate circumstellar from photospheric features, it is important to have estimates of both the stellar rotational velocity ($v \sin i$) and the radial velocity (RV) of the object relative to the barycenter. For many of the objects in our sample these values have been estimated in the literature. For objects that do not have previous estimates, we fit rotationally broadened and velocity-shifted synthetic spectra to a single spectral order to obtain RV and $v \sin i$ estimates. The order selected is chosen based on the strongest available photospheric lines. This method works well for A-type and late B-type objects but fails for the earliest spectral types. Typically the strong He I $\lambda 4471$ and Mg II $\lambda 4481$

lines are used to measure $v \sin i$ for rapidly rotating B-type stars (Halbedel 1996); for more slowly rotating B-type stars, metal lines near 6400 \AA and 4500 \AA are used (Fekel 2003). Many of our early type objects, however, show no absorption features at any of these wavelengths. For a typical S/N spectrum in our sample, this method can also fail for stars with $v \sin i \gtrsim 200 \text{ km s}^{-1}$ because the features become too weak to reliably measure. Lower resolving powers of $R \sim 10,000$ - $30,000$ are typically used to measure the large $v \sin i$ values of B-type stars (e.g. Halbedel 1996). We do not obtain $v \sin i$ estimates for these objects.

For objects that do not have literature or synthetic spectrum fit RV estimates, we use the interstellar Na I D lines as an RV proxy. Finkenzeller & Jankovics (1984) were the first to show, using a sample of 10 HAEBES, that the velocities of the molecular clouds in which HAEBES are embedded are very similar (mean residual of $-3.1 \pm 3 \text{ km s}^{-1}$) to the velocities of observed interstellar Ca II and Na I D velocities in the same objects. They also showed that independently measured stellar RVs were similar to the molecular cloud velocities, although with a larger mean residual of $8.5 \pm 8 \text{ km s}^{-1}$. Thus the Na I D velocities can, in general, provide a rough estimate of the stellar RV to within $\sim 10 \text{ km s}^{-1}$. As the mass flow diagnostics we are interested in are typically several hundred km s^{-1} wide, this is adequate for our purposes.

For objects in our sample for which we determine RVs based on synthetic spectrum fits, we compare these measurements to the RV determined from the object's interstellar Na I D lines. RVs determined by the synthetic spectral fits from Alecian et al. (2013) are also used. The interstellar Na I RV estimate is made by manually pointing at the approximate center of the interstellar absorption. This is appropriate since the estimates are only accurate to $\sim 8 \text{ km s}^{-1}$. An example of the Na I interstellar medium (ISM) absorption is shown in Figure 1 for HD 142666. The Na I ISM absorption is very strong and narrow and is clearly distinguished from the photospheric profile. This is a particularly good example of the strength of using the Na I value as an estimate for the system RV: the Na I and synthetic model values differ by only $\sim 2.5 \text{ km s}^{-1}$. Further examples of the Na I ISM features can be seen in the individual object plots in the Appendix.

The result of the comparison is plotted in Figure 2. Most objects show a velocity discrepancy of $< 10 \text{ km s}^{-1}$. The four objects that lie outside of the 20 km s^{-1} boundaries are all confirmed binaries and the large velocity differences may be due in part to their orbital motion. We find a mean velocity difference of $8.1 \pm 3.6 \text{ km s}^{-1}$ for the objects in Figure 2, where the uncertainty is the 95% confidence interval given by the t -distribution (Feigelson & Babu 2012). The mean difference drops to 7.9 km s^{-1} if the four outliers are excluded, a negligible difference. The standard deviation of the absolute value of the difference between the interstellar RV values and those determined by the model fits is 8.5 km s^{-1} . We take this to be the uncertainty associated with the values determined from the Na I lines.

Our sample thus confirms the findings of Finkenzeller & Jankovics (1984). For future HAEBE studies we sug-

gest that the interstellar Na I D line velocities be used for objects that, (1) do not allow for reliable photospheric fits either due to lack of absorption features or very high $v_{\text{sin}i}$, or (2) only $\sim 10 \text{ km s}^{-1}$ accuracy is needed in the radial velocity. All other physical information about the

objects examined in this study (e.g. M_* , R_* , \dot{M}) are taken from the literature. The relevant references are given in [Table 2](#).

Table 2
HAEBE optical sample physical parameters^a

Object ID (1)	Spectral Type (2)	v_{rad} (km s^{-1}) (3)	M_* (M_{\odot}) (4)	R_* (R_{\odot}) (5)	$v_{\text{sin}i}$ (km s^{-1}) (6)	$\log(\dot{M})$ ($M_{\odot} \text{ yr}^{-1}$) (7)	Disk Detected ^b (8)	i ($^{\circ}$) (9)	References (10)
AB Aur	A0	24.7	2.50	2.62	116	-6.85	Y	40	1,2
AE Lep	B6	28.0	39
BD+61 154	B8	-16.0	3.40	2.42	112	...	Y	70	1,6,9
BF Ori	A2	22.0	2.58	3.26	39	<-8.00	Y	...	1,2,6,8
BH Cep	F5	-5.6	1.70	2.40	98	<-8.30	Y	84	2,38,40
CQ Tau	F2	35.7	2.93	5.10	98	<-8.30	Y	29	1,2,12,37
DW CMa	B3	Y	...	4,13
GSC 04794-00827	A?	25.0	43
HD 141569	A0	35.7	2.33	1.94	228	-6.90	Y	55	1,2,14
HD 142666	A5	-9.7	2.15	2.82	65	-7.22	Y	...	1,3,15
HD 163296	A1	-9.0	2.23	2.28	129	-7.16	Y	...	1,3,6,18
HD 169142	A7	-0.4	1.69	1.64	48	...	Y	0	1,46
HD 190073	A1	0.2	2.85	3.60	4	...	Y	45	1,19
HD 203024	A1	-14.0	2.80	3.40	162	...	Y	74	1,44
HD 244314	A1	22.5	2.33	2.07	52	-6.90	1,3
HD 244604	A4	26.8	2.66	3.69	98	-7.20	Y	...	1,3,21
HD 245185	A1	16.0	2.19	1.85	118	-7.20	Y	81	1,3,6,44
HD 249879	A2	11.0	4.00	5.90	249	-8.00	1,3
HD 250550	B8	-22.0	4.80	3.50	79	-7.80	Y	...	1,3,13
HD 287823	A0	-0.3	2.50	2.60	10	...	?	...	1
HD 290409	A2	80.3	2.04	1.75	250	1
HD 290500	A2	29.0	1.96	1.68	85	1
HD 290764	A8	26.3	1.86	2.30	60	...	Y	32	41
HD 290770	B9	24.6	2.86	2.49	240	1
HD 34282	A3	16.2	1.59	1.66	105	<-8.30	Y	...	1,2,18,22
HD 35187	A2	27.0	1.93	1.58	93	-7.60	Y	...	1,3,24
HD 35929	F1	21.1	4.13	8.10	61.8	...	Y	56	1,44
HD 36408	B8	15.0	4.10	3.50	...	<-8.00	?	...	2
HD 37357	A1	21.4	2.47	2.83	124	...	Y	...	1,47
HD 37411	B9	14.1	Y	63	33,44
HD 38120	B9	28.0	2.49	1.91	97	-6.90	Y?	<8	1,3,35
HD 50083	B4	-0.5	12.10	10.0	233	...	?	...	1
HK Ori	A3	22.9	3.00	4.10	20	-5.24	Y	...	2,6
IL Cep	B4	-39.0	179	...	?	...	1
IP Per	A3	13.7	1.86	2.10	80	...	?	...	1
IRAS 05044-0325	B3	25.2	43
IRAS 06071+2925	B9	12.5	43
IRAS 07061-0414	B0	43.0	42
IRAS 17481-1415	A0	-5.1	2.50	10
IRAS 18306-0500	B2	33.1	12.00	6.80	Y	87	40,44
IRAS 18454+0250	B1	~ 0	19.00	8.50	42,13
IRAS 19343+2926	B1	-10.7	43
LkH α 134	B3	-13.0	6.00	5.05	Y	58	40,44
LkH α 208	A4	13.6	2.40	3.20	Y	56	40,44
LkH α 233	A3	-9.10	3.20	4.45	Y	18	40,44
LkH α 257	B5	-15.2	3.61	2.68	Y	57	44
LkH α 324	B8	-10.5	5.10	6.30	Y	42	40,44
LkH α 339	A1	26.4	3.18	3.92	Y	40	40,44
MWC 1080	B1	...	17.4	7.3	Y	83	1,6,10
MWC 120	B9	47.0	3.94	4.60	120	-6.85	Y	...	1,3
MWC 137	B1	Y	80	6,10,13
MWC 147	B2	18.6	6.60	4.80	83	-6.12	Y	...	1,3,13,48
MWC 300	B1	-4.5	7.37	3.33	Y	62	13,44
MWC 361	B4	-7.0	10.70	10.40	26	...	Y	26	1,44
MWC 480	A4	12.9	1.93	1.93	98	<-7.23	Y	37	1,2,12
MWC 610	B3	14.0	8.00	4.70	219	...	?	...	1
MWC 614	A0	15.1	69	-6.59	Y	...	1,3,28
MWC 758	A5	17.8	2.90	4.40	54	-6.05	Y	21	1,3,12
MWC 778	B2	10.3	10.00	3.50	Y	75	13,42,49
MWC 863	A1	-5.0	2.56	2.89	108	-6.12	Y	38	1,2,29
NZ Ser	B3	-17.0	10.10	5.80	Y	5	10,13
R Mon	B8	22.3	5.10	12.00	Y	60	10,13
RR Tau	A0	15.3	5.80	9.30	225	-6.86	Y	44	2,32,44
SV Cep	A1	24.6	2.62	3.00	180	...	Y	49	1,44
T Ori	A3	56.1	3.13	4.47	147	-6.60	Y	...	1,2,30
UX Ori	A1	12.0	6.72	12.1	221	-7.18	Y	<8	1,3,6,35

Table 2 — Continued

Object ID (1)	Spectral Type (2)	v_{rad} (km s ⁻¹) (3)	M_* (M_\odot) (4)	R_* (R_\odot) (5)	$vsini$ (km s ⁻¹) (6)	$\log(\dot{M})$ (M_\odot yr ⁻¹) (7)	Disk Detected ^b (8)	i ($^\circ$) (9)	References (10)
UY Ori	B9	19.8	4
V1185 Tau	A2	20.0	250
V1578 Cyg	A1	-3.0	5.90	9.70	199	...	Y	...	1,6
V1685 Cyg	B4	-16.0	Y	41?	30,34
V1686 Cyg	F8	-12.2	3.50	14.00	Y	...	6,40
V1787 Ori	A5	26.4	1.88	1.84	...	-7.43	45
V1818 Ori	B7	26.4	46	43
V346 Ori	A7	20.0	1.72	1.96	116	-6.90	N?	...	1,3,35
V351 Ori	A6	15.0	2.88	4.38	100	...	?	...	1
V361 Cep	B4	-20.0	8.11	6.70	278	...	N?	...	1,6
V373 Cep	B8	-18.6	5.30	14.00	Y	45	39,40
V374 Cep	B5	-13.6	51
V380 Ori	B9	27.5	2.87	3.00	7	-5.60	Y	...	1,3,6
V586 Ori	A1	31.0	2.28	1.94	200	...	Y	81	1,44
V590 Mon	B7	17.7	4.71	5.86	84	40,44
V599 Ori	F0	7.0	1.83	5.29	96	...	Y	42	43,44
V718 Sco	A4	-3.6	1.93	2.25	113	...	Y?	32?	1,35
V791 Mon	B5	-2.6	?	...	4
VV Ser	B7	-2.0	4.00	3.10	124	-7.50	Y	46	1,3,44
WW Vul	A2	-4.0	3.70	5.40	196	-6.38	1,2
XY Per	A2	2.0	1.95	1.65	224	-7.02	?	...	1,3
Z CMa	B9	-27.0	3.80	3.20	...	-6.72	Y	...	3,31

Note. — References: 1=Alecian et al. (2013), 2=Mendigutía et al. (2011), 3=Donehew & Brittain (2011), 4=Vieira et al. (2003), 5=Carmona et al. (2010), 6=Hillenbrand et al. (1992), 7=Tang et al. (2012), 8=Finkenzeller & Mundt (1984), 9=Bossier et al. (2011), 10=Alonso-Albi et al. (2009), 11=Guilloteau et al. (2011), 12=Guilloteau et al. (2013), 13=Verhoeff et al. (2012), 14=Thi et al. (2014), 15=Schegerer et al. (2013), 16=Eisner et al. (2009), 17=Chen et al. (2012), 18=Marínas et al. (2011), 19=Ragland et al. (2012), 20=Okamoto et al. (2009), 21=Vink et al. (2002), 22=Natta et al. (2004), 23=Acke & van den Ancker (2004), 24=Oudmaijer et al. (1992), 25=Fuente et al. (2002), 26=Millan-Gabet et al. (2001), 27=Perrin et al. (2006), 28=Liu et al. (2007), 29=Fukagawa et al. (2003), 30=Eisner et al. (2004), 31=Schütz et al. (2005), 32=García Lopez et al. (2006), 33=Mal-fait et al. (1998), 34=Hernández et al. (2004), 35=Dent et al. (2005), 36=Corporon & Lagrange (1999), 37=Mendigutía et al. (2011), 38=Liu et al. (2011), 39=Lee & Chen (2009), 40=Manoj et al. (2006), 41=Kraus et al. (2013), 42=Reed (2003), 43=Sartori et al. (2010), 44=Liu et al. (2011), 45=Caratti o Garatti et al. (2012), 46=Osorio et al. (2014), 47=Juhász et al. (2010), 48=Bag-noli et al. (2010), 49=Perrin et al. (2009), 50=Acke et al. (2005), 51=Thé, de Winter, & Pérez (1994)

^a All spectral types, values of M_* , R_* , \dot{M} , i , and disk detections are taken from the literature. Values of the radial velocity and $vsini$ determined in this study are given in bold. Typical radial velocity uncertainties are ~ 5 – 10 km s⁻¹; typical $vsini$ uncertainties are ~ 5 – 10 km s⁻¹ although large values of $vsini$ can have uncertainties as large as 30–100 km s⁻¹.

^b Disk detections are indicated to provide context for the line profiles presented in this study. Question marks (?) indicate that the measurements are uncertain as to whether or not a disk is present. The detections are taken from the literature and are based mainly on millimeter and near-IR flux measurements (see given references).

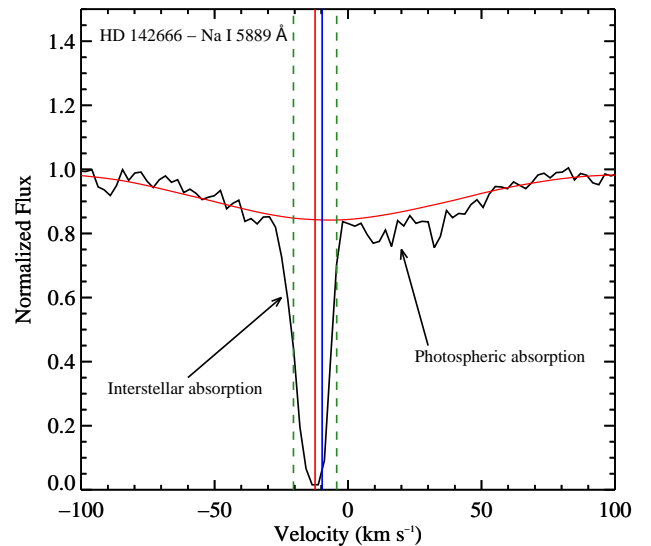


Figure 1. Comparison of the interstellar Na I RV determination with the value calculated from fitting a synthetic spectrum to photospheric absorption lines for HD 142666. The observed profile is shown in black; the broadened spectroscopic standard HR 3221 is over plotted in red. The RV value estimated from the ISM feature is shown with the vertical red line. The photospheric model fit RV is shown with the vertical blue line. The ± 8.5 km s⁻¹ uncertainty for the Na I value is shown with the vertical green dashed lines. It is clear that manually selecting the center of the ISM absorption results in negligible errors compared with the systematic uncertainty of using the Na I to estimate the system RV.

4. PROFILE CLASSIFICATION

Line profiles are classified into six morphological groups: P-Cygni (PC), inverse P-Cygni (IPC), double-peaked emission (DP), single-peaked emission (E), absorption (A), and featureless (F). For the purpose of generating mass flow statistics, pure absorption profiles

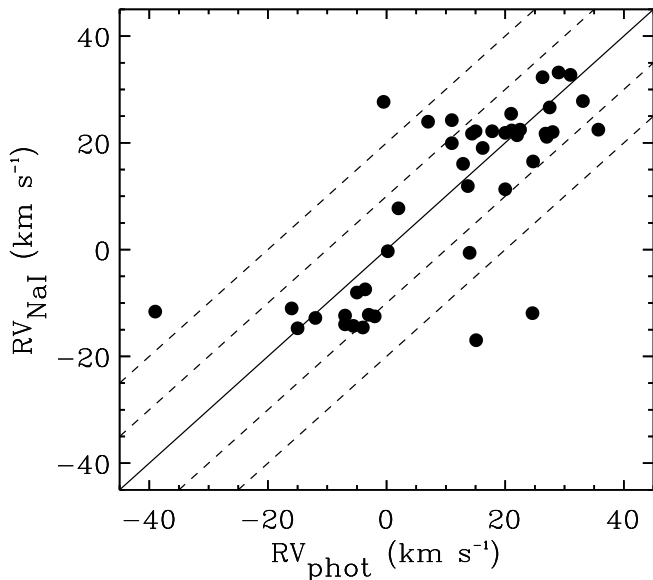


Figure 2. Radial velocities calculated from synthetic model photosphere fits versus Na I D interstellar absorption velocities. The solid line represents equal velocities. The dashed lines moving outward from the solid line represent differences between the velocities of 10 and 20 km s^{-1} . The mean deviation is 8.1 km s^{-1} . We note that the four objects (HD 50083, IL Cep, MWC 614, and SV Cep) lying outside of the 20 km s^{-1} boundary are all known binaries. The large velocity discrepancies in these objects may be due to their orbital motion.

(A) are further grouped as red or blue absorption based on the maximum absorption velocity: $v_{red} > 0 \text{ km s}^{-1}$ and $v_{blue} < 0 \text{ km s}^{-1}$. The objects counted as showing blue(red)-shifted absorption either have a PC(IPC) profile *or* an A profile that is blue(red)-shifted. Objects are classified as E or DP if the profile is in emission (single and double peaked, respectively) and there is no clear evidence of absorption below the local continuum. Profiles are labeled as F if they show no detectable departure from the estimated photospheric line profile. We note that a small number of the PC profiles, most of them $H\alpha$ profiles, show blue-shifted absorption that does not extend below the stellar continuum, i.e., the absorption is superposed on the wing of the emission profile (see, for example, the $H\alpha$ profile in [Figure 3](#)). While these are not strictly P-Cygni profiles, we have chosen to extend the PC classification to these objects since it is the closest morphology group that describes the profile.

In order to accurately classify the morphologies, each profile was compared with a rotationally broadened spectroscopic standard of a similar effective temperature. Objects with unknown $v \sin i$ values did not have their comparison spectra broadened. For most objects, this allowed weak emission and absorption features to be identified in lines with significant photospheric components. This comparison is most important for the Balmer lines since most of our objects have strong photospheric Balmer line absorption. An example of this effect is shown in the top panel of [Figure 5](#) where the core of the $H\gamma$ profile of HD 190073 is clearly filled in by emission. A second example is shown in the bottom panel of [Figure 5](#) for a more complex line morphology at $H\beta$ for HD 290770. In this case the blue-shifted absorption at $\sim 100\text{--}200 \text{ km s}^{-1}$ can clearly be seen superimposed

on the broad emission profile. The comparison with the standard makes it obvious that this is non-photospheric absorption. To be clear, we note that the profiles shown in [Figure 3](#) and [Figure 4](#) show only the continuum normalized profiles—no photospheric subtraction was done to make these plots even though photospheric comparisons were made while classifying the profiles. The photospheric comparisons are done by eye and, in general, it is obvious when a non-photospheric contribution to the line profile is present. Thus no quantitative comparison of the photospheric and circumstellar components is performed. The approximate comparisons prevent gross misclassification of line profiles, i.e. identifying circumstellar absorption when the absorption actually forms in the photosphere. Thus objects will often show line profiles that appear to show structure but are in fact due entirely to photospheric absorption. Examples of an A0 and B3 spectroscopic standard are shown in [Figure 6](#) and [Figure 7](#).

In some objects there is significant contamination of the He I 3889 Å, Mg I 5167 Å, Ca II 3969 Å, and Ca II 8662 Å spectral lines by neighboring features. This is especially severe at Mg I 5167 Å (e.g. Z CMa and DW CMa), where we tentatively identify the nearby Fe I 5168.89 Å line ($+81.8 \text{ km s}^{-1}$), and Ca II 3969 Å and He I 3889 Å which are often overwhelmed by the nearby He and $H\zeta$ lines, respectively. For example, in [Figure 3](#) the He I 3889 Å line appears to show a PC morphology. However, this profile more likely due to the nearby $H\zeta$ line. Thus this line is listed as “contaminated” since the true profile is obscured by the $H\zeta$ line. The N II 6548 Å line lies in the far blue wing of the $H\alpha$ and often appears to show structure when in fact the line emission and shape are due entirely to $H\alpha$ (e.g., [Figure 3](#)). If there are other lines of the same element that show a non-featureless line profile, e.g. the Mg I 5173 or 5184 Å lines in the case of Mg I 5167 Å, the line is categorized as ‘C’ for ‘contaminated’. If the other lines of the same element are featureless, we assume a featureless spectrum for the feature in question. The rest velocities of these contaminating lines are marked with a dotted line in the individual profiles plots. With the exception of Ca II 8662 Å, the wavelength regions containing these diagnostics are mostly featureless in the whole sample. Contaminated profiles comprise 16% of the He I 3889 Å profiles, 3% of the Mg I 5167 Å profiles, 7% of the Ca II K profiles, and 9% of the Ca II 8662 Å profiles. Thus the contamination is not problematic concerning the classification of most profile morphologies.

Examples of the extracted profiles and their categorization are shown in [Figure 3](#) and [Figure 4](#). Plots of the individual line profiles for all objects are given in Appendix A. The profile classification is shown in the upper right corner of each plot window; the spectral feature being shown is listed in the upper left. Spectral lines for which there is no data are labeled as such in the plots. These lines either fell in between orders on the detector or the S/N was too low for analysis. Features with rest wavelengths below 5000 Å are plotted using a 5 km s^{-1} (2 pixel) bin window in order to enhance the S/N. The bottom-right panel of each figure shows a bar plot of the number of line profiles in each morphology category. We

note that only the PC and IPC bars are shown in color. The bar showing the count for pure red- or blue-shifted absorption (i.e., the A profiles) is shown in black even though the subdivision of the A profiles into red- and blue-shifted absorption is included in the statistics.

5. MORPHOLOGY STATISTICS

5.1. Pre-main sequence evolutionary groups

HAEBES display a wide variety of SEDs indicating that, as a group, they represent objects at different phases of pre-main sequence evolution (Meeus et al. 2001; Malfait et al. 1998; Hillenbrand et al. 1992). An accurate calculation of mass flow statistics would only include objects that are currently in the same pre-main sequence phase as one another. However, this is challenging due to the relatively small number of HAEBES each specific evolutionary phase would contain. Studies of this sort will necessarily suffer from smaller sample sizes in each group thus increasing the uncertainties associated with the mass flow statistics.

In order to eliminate any objects from our sample that no longer show evidence of inner disk material, and thus should not show evidence of mass accretion and mass loss, we employ the color-color classification of Hillenbrand et al. (1992). The $J - H$ vs $H - K$ classification is a proxy for the full SED analysis presented in Hillenbrand et al. (1992). Objects with $J - H < 0.3$ and $H - K < 0.3$, the Group III objects from Hillenbrand et al. (1992), likely have insufficient material in their inner disks to be actively accreting and ejecting material. These objects should not be included in any comparisons to CTTSs since all CTTSs show strong evidence for accretion and mass loss.

We have collected J , H , and K data from the literature for our observed sample in order to identify any potential Group III objects. Optical extinctions are also collected for some objects. The $J - H$ and $H - K$ colors for our sample are plotted in Figure 8. Objects with de-reddened colors are plotted as green circles while objects without known A_V values are plotted as red squares. Reddening vectors for the standard $R=3.1$ extinction law are plotted as solid black lines. An approximation of the main sequence for dwarf spectral types B8 through M6 is represented by the dashed-dotted line. Main sequence objects are required to remain within the boundaries of the reddening vectors. It can be seen that most of our objects lie well to the right of the main sequence region, confirming the existence of significant excess emission. The Group III objects from Hillenbrand et al. (1992) all exist in region $J - H < 0.3$, $H - K < 0.3$. We use the box defined by the intersection of these boundaries as our criteria for identifying Group III objects in our sample. The box is plotted in Figure 8 using dashed lines. There are 9 objects (AE Lep, HD 141569, HD 203024, HD 35929, HD 36408, HD 50083, IL Cep, MWC 610, and V361 Cep) that lie within the Group III box. These objects are marked with a † in Table 4 and will be excluded from the analysis presented in the rest of the paper. This reduces the sample to 78 objects.

5.2. Calculating the mass flow incidence

In order to exclude objects that are not unambiguously experiencing some sort of outflow or accretion, we

do not include pure emission lines (double or single-peaked) as evidence of mass flows. While emission lines in many species can form in a wind or accretion flow, they can also form in static geometries such as extended stellar and disk atmospheres or remnant circumstellar envelopes. On the other hand, doppler shifted absorption is an unambiguous sign of mass motion. The CTTS comparison statistics that are discussed in subsection 5.5 are calculated using the same criteria. Thus we only count red and blue-shifted absorption below the local continuum (e.g. the blue-shifted absorption seen at $H\beta$ in the bottom panel of Figure 5) as indications of mass flows when calculating the final statistics in Table 3 and Table 4. For objects with multiple observations ($\sim 20\%$ of the sample, see Table 1) we search for absorption signatures in all of the exposures. Thus the computed statistics include objects that, for example, show blue-shifted absorption in a line for one exposure but do not show the same morphology in a separate exposure. This enables us to account for variability, in a limited way, in at least some objects.

The morphology statistics for the mass flow diagnostics are presented in Table 3 and a summary of each object's profile classifications is given in Table 4. In Table 3 the line diagnostic with the highest occurrence of each profile type is highlighted in bold font. For each line the total number of object profiles examined is given in column 2. The number of each type of morphology is listed and the fraction of the total number of profiles is given in parentheses. In column 8 of Table 4 the total number of line diagnostics examined is given for each object. The number of contaminated profiles for each object is not shown although they are included in the total number of lines in column 8. It is immediately obvious from Table 3 that most of the diagnostics show featureless profiles. In fact, $H\alpha$, $H\beta$, and Ca II $\lambda 8498$ are the only lines for which a majority of the sample displays some form of activity. The lines with the highest incidence of circumstellar features displaying PC and IPC morphologies are $H\beta$ (30%) and He I $\lambda 5876 \text{ \AA}$ (14%), respectively. The Na I D lines show the highest rate (12%) of pure absorption profiles. After the Balmer lines, the next best spectral line for observing a PC morphology is Fe II $\lambda 4924$ which displays PC characteristics in 11% of the object profiles.

The last row in Table 4 displays the final mass flow statistics for our sample. The uncertainties are the 68% confidence intervals calculated using Wilson's score test for large samples (Wilson 1927). These intervals are very close to the values obtained assuming Poisson statistics in the distribution of observed incidence. However, the Wilson score test results in a weighted average towards the center of the distribution. We note that the given incidence is not the adjusted fraction given by the score test and thus the confidence intervals may be asymmetric around the value. The occurrence of both inflow and outflow signatures in our sample are fairly low: only 26% of our objects have at least one profile displaying red-shifted absorption; only 37% have at least one profile displaying blue-shifted absorption.

5.3. Comparison to previous HAEBE studies

A comparison of our mass flow statistics to previous HAEBE studies is presented in Table 5. We find simi-

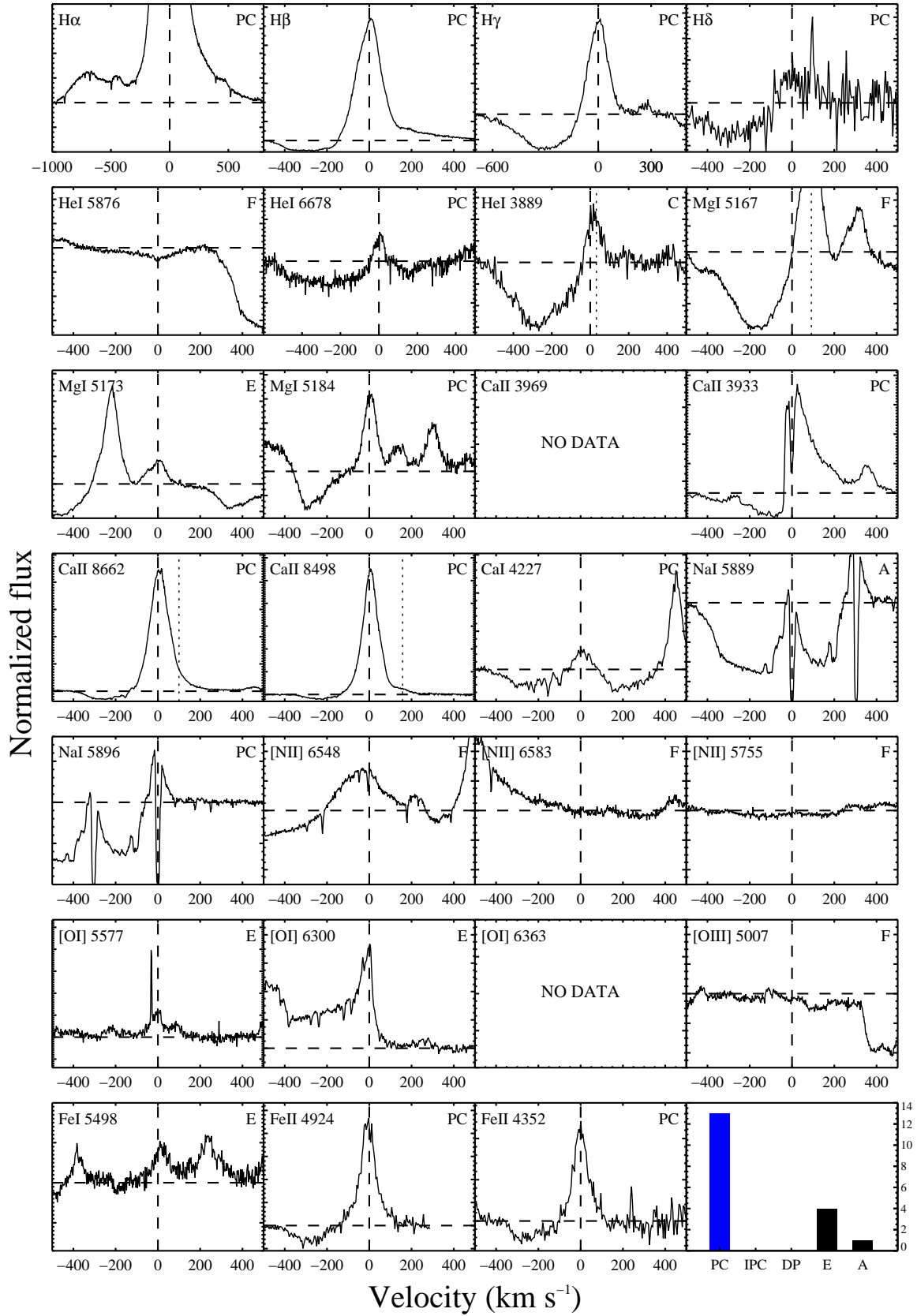


Figure 3. Extracted line profiles for Z CMA. The continuum, which is normalized to 1.0, is marked with a horizontal dashed line. The stellar rest velocity is marked with a vertical dashed line. The profile classification is noted in the upper-right of each plot window. The plotted spectral line is listed in the upper-left. The bottom right-most plot window is a bar plot of the profile types for the object. The featureless profile count is excluded from the bar plot. Z CMA displays strong outflow signatures in numerous lines. The H α vertical plot range is abbreviated to show the blue-shifted absorption. The [NII] 6548 Å appears to show emission but is actually showing the far blue wing of the H α line. Although the Na I doublet lines should show scaled versions of the same profile morphology, the blue-shifted absorption from the 5896 Å profile decreases the prominent peak of the 5889 Å profile to below the local continuum, resulting in a classification of ‘A’ for the 5889 Å line. Note the vertical dotted lines denoting the rest wavelengths of lines that potentially contaminate the line of interest (e.g., H ζ in the He I 3889 Å panel).

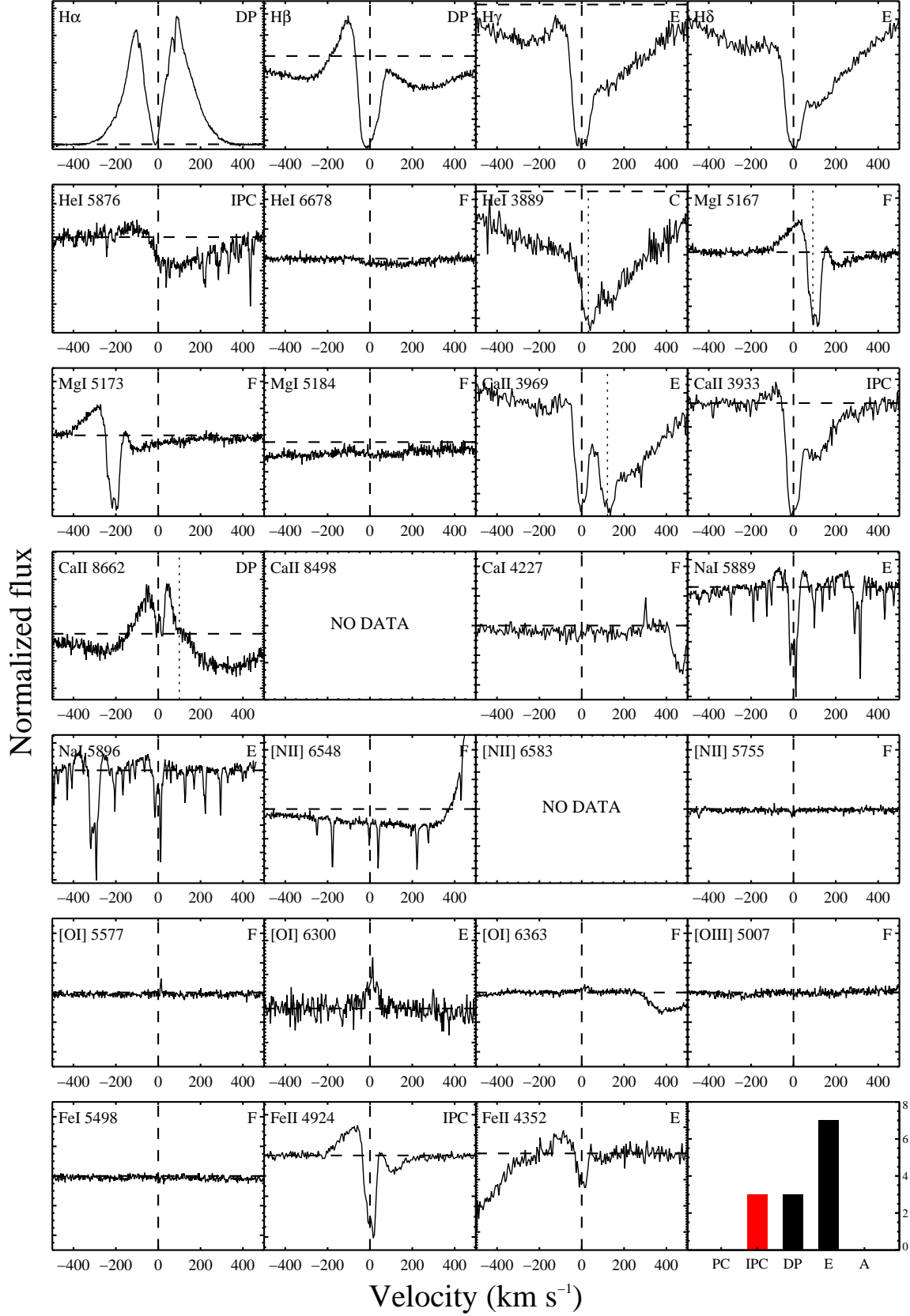


Figure 4. Extracted line profiles for MWC 120. The format is the same as [Figure 3](#). Note the strong IPC morphology in the He I 5876 Å line.

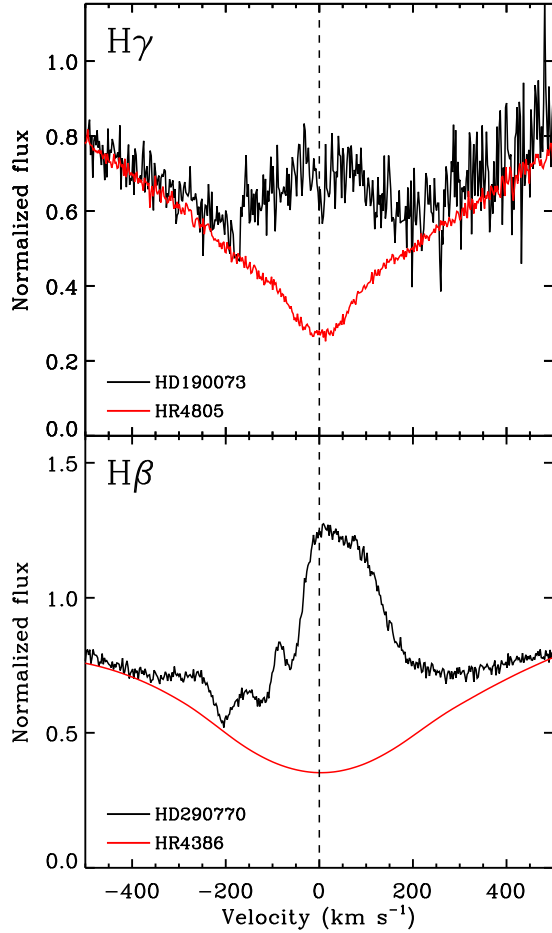


Figure 5. A comparison of the $H\gamma$ profile of HD 190073 with a spectroscopic standard of similar T_{eff} (top panel). The object profile is plotted in black and the standard photospheric profile is plotted in red. The core of the line is clearly filled in by emission, placing this profile in the E morphology group. A similar comparison is shown for HD 290770 (bottom panel) at $H\beta$. The standard, HR4386, has been rotationally broadened to match the $v\sin i$ of HD 290770. The blue-shifted absorption can be seen superimposed on the emission profile, resulting in a profile classification of PC.

lar rates of blue-absorption in our sample compared to both Finkenzeller & Mundt (1984, FM84) and Hamann & Persson (1992, HP92). Both Vieira et al. (2003, V03) and Reipurth et al. (1996, R96) find rates of blue-shifted absorption that are significantly lower than ours (as well as FM84’s and HP92’s). We attribute this large discrepancy to the fact that they only observe $H\alpha$ which tends to mask sub-continuum absorption due to strong emission components from multiple sources (e.g. emission from accretion, stellar winds, nebular background). We note, however, that using solely $H\alpha$ in our sample results in a blue-shifted absorption fraction of $26\%_{-4}^{+5}$, a value in between the low rates of Vieira et al. (2003) and Reipurth et al. (1996) and our final fraction (37%). This may be due to our classification of profiles as P-Cygni if the blue feature is clearly absorption and not a second peak, even if the absorption does not extend below the local emission continuum (e.g. Figure 5). Our results, and those of FM84 and HP92, show that in order to recover accurate outflow statistics diagnostics other than $H\alpha$ should be examined. The line with the largest occurrence of blue-absorption in our sample is $H\beta$ (30%), although the incidence in $H\alpha$ is similar at 26%. In fact, all objects in our sample that show P-Cygni type profiles in lines other than $H\alpha$ and $H\beta$ also show P-Cygni morphologies in either $H\alpha$ or $H\beta$. Thus it appears $H\beta$ is a very strong stand-alone diagnostic of outflows in HAEBES.

Table 3
Line morphology statistics

Line ID (1)	Total (2)	Profile morphology					
		PC (3)	IPC (4)	DP (5)	E (6)	A (7)	F (8)
$H\alpha$	78	20(.26)	5(.06)	34(.44)	17(.22)	0(.00)	2(.03)
$H\beta$	74	22(.30)	4(.05)	15(.20)	18(.24)	5(.07)	10(.14)
$H\gamma$	61	12(.20)	0(.00)	0(.00)	3(.05)	14(.23)	3(.05)
$H\delta$	51	5(.10)	0(.00)	1(.02)	8(.16)	5(.10)	32(.63)
He I λ 3889	49	0(.00)	0(.00)	0(.00)	1(.02)	0(.00)	40(.82)
He I λ 5876	78	1(.01)	11(.14)	1(.01)	11(.14)	1(.01)	53(.68)
He I λ 6678	71	1(.01)	1(.01)	0(.00)	2(.03)	1(.01)	66(.93)
Mg I λ 5167	71	0(.00)	0(.00)	0(.00)	0(.00)	0(.00)	69(.97)
Mg I λ 5173	71	0(.00)	0(.00)	0(.00)	3(.04)	0(.00)	68(.96)
Mg I λ 5184	71	1(.01)	0(.00)	0(.00)	5(.07)	0(.00)	65(.92)
Ca II λ 3933	57	2(.03)	1(.01)	0(.00)	1(.01)	4(.05)	65(.89)
Ca II λ 3969	42	0(.00)	0(.00)	0(.00)	3(.07)	1(.02)	35(.83)
Ca II λ 4227	71	1(.01)	0(.00)	0(.00)	0(.00)	0(.00)	70(.99)
Ca II λ 8498	27	2(.07)	1(.04)	2(.07)	9(.33)	0(.00)	13(.48)
Ca II λ 8662	70	2(.03)	2(.03)	3(.04)	22(.31)	0(.00)	35(.50)
Na I λ 5889	78	4(.05)	1(.01)	0(.00)	19(.24)	9(.12)	45(.58)
Na I λ 5896	78	4(.05)	1(.01)	0(.00)	18(.23)	8(.10)	47(.60)

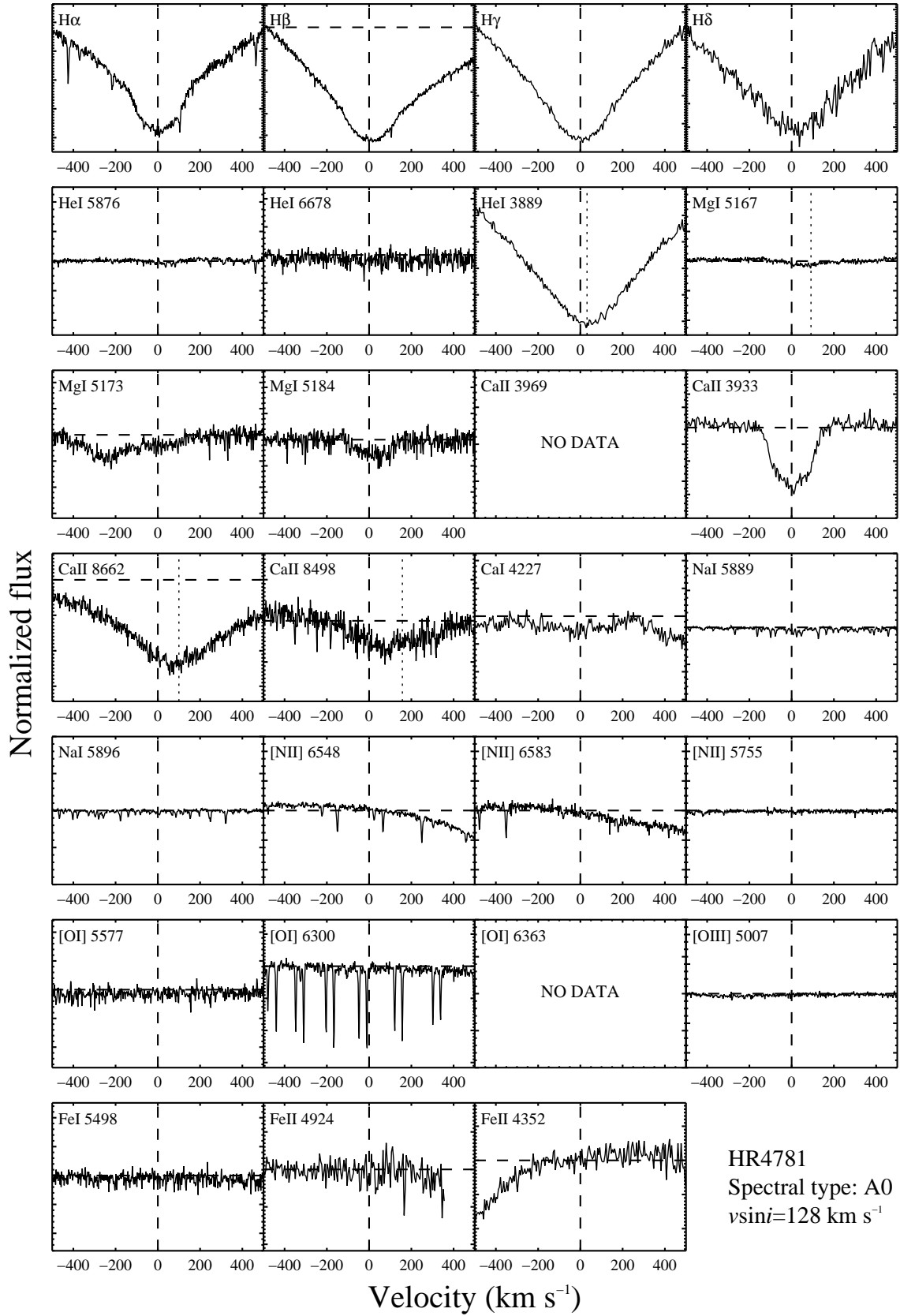


Figure 6. Extracted line profiles for the spectroscopic standard HR 4781.

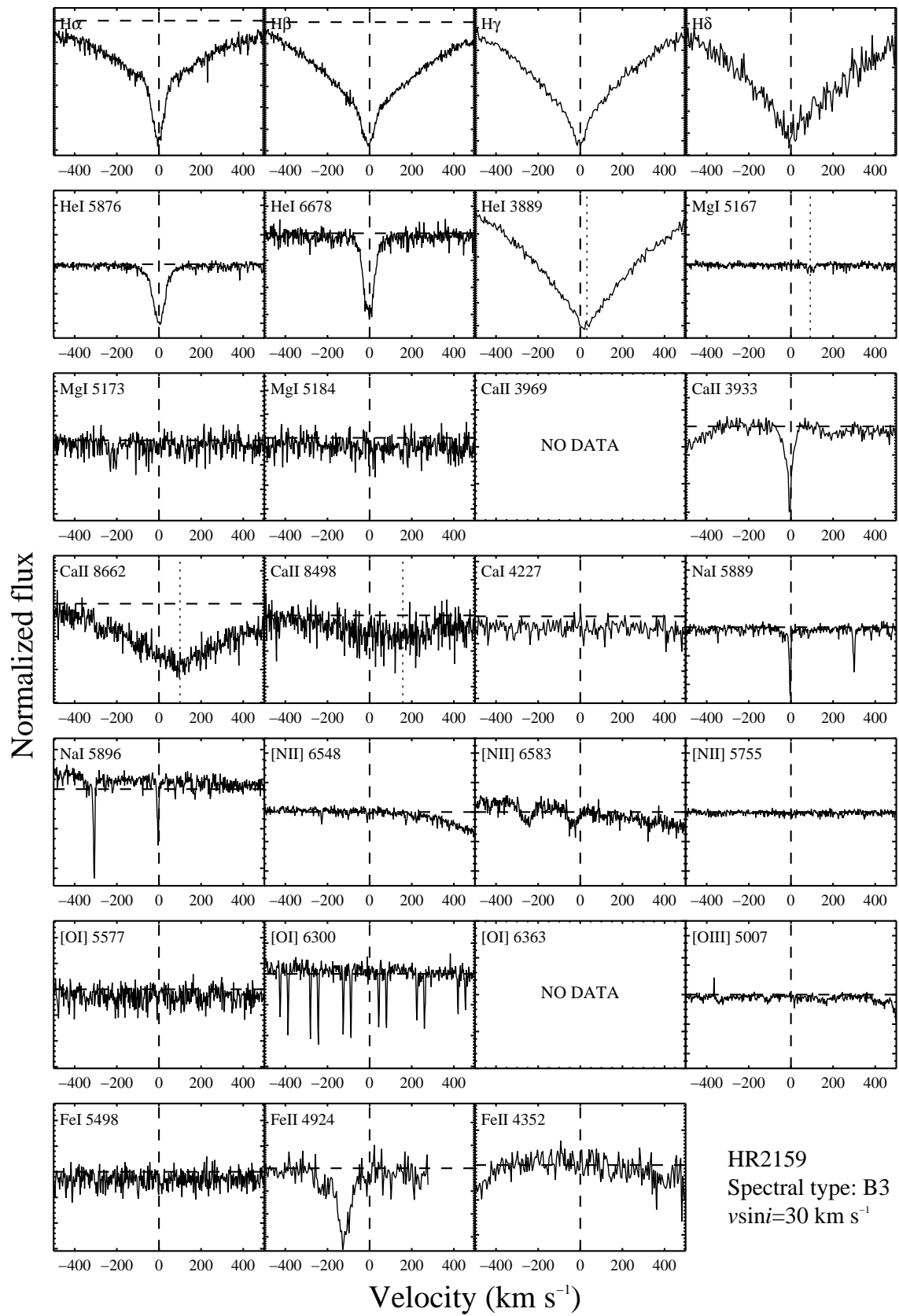


Figure 7. Extracted line profiles for the spectroscopic standard HR 2159.

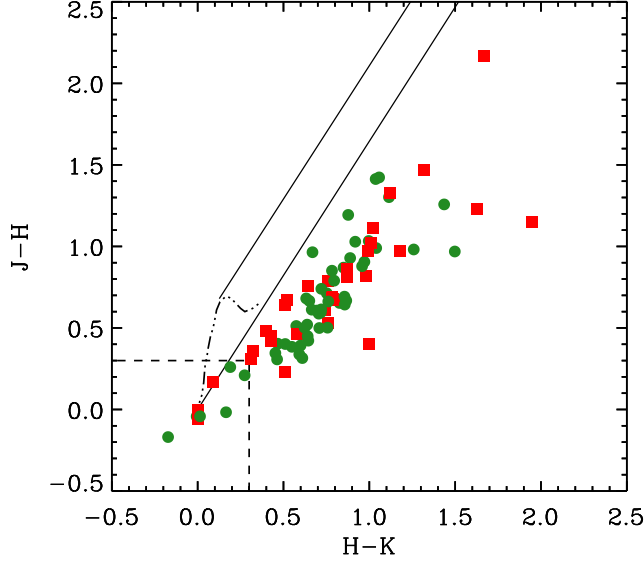


Figure 8. $J - H$ and $H - K$ colors for our sample. Reddening vectors are plotted as solid lines. The approximate location of the main sequence is indicated by the dashed-dotted line. The area within the dashed lines contains objects that are most likely evolved HAEBS without any significant IR excess. Objects with de-reddened colors are plotted as green circles; objects without reddening corrections are plotted as red squares. There are 9 objects contained in the box that we exclude from further analysis.

Table 3 — *Continued*

Profile morphology							
Line ID (1)	Total (2)	PC (3)	IPC (4)	DP (5)	E (6)	A (7)	F (8)

Table 3 — *Continued*

Profile morphology							
Line ID (1)	Total (2)	PC (3)	IPC (4)	DP (5)	E (6)	A (7)	F (8)

Table 3 — *Continued*

Profile morphology							
Line ID (1)	Total (2)	PC (3)	IPC (4)	DP (5)	E (6)	A (7)	F (8)
[N II] $\lambda 5755$	78	0(.00)	0(.00)	0(.00)	3(.04)	0(.00)	75(.96)
[N II] $\lambda 6548$	78	0(.00)	0(.00)	0(.00)	2(.03)	0(.00)	76(.97)
[N II] $\lambda 6583$	40	0(.00)	0(.00)	0(.00)	6(.15)	0(.00)	34(.85)
[O I] $\lambda 5577$	78	0(.00)	0(.00)	0(.00)	6(.08)	0(.00)	72(.92)
[O I] $\lambda 6300$	77	0(.00)	0(.00)	0(.00)	43(.56)	0(.00)	34(.44)
[O I] $\lambda 6363$	64	0(.00)	0(.00)	0(.00)	20(.31)	0(.00)	44(.69)
[O II] $\lambda 5007$	71	0(.00)	0(.00)	0(.00)	3(.04)	0(.00)	68(.96)
Fe I $\lambda 5498$	78	0(.00)	0(.00)	0(.00)	1(.01)	0(.00)	77(.99)
Fe II $\lambda 4924$	64	7(.11)	2(.03)	1(.02)	7(.11)	3(.05)	44(.69)
Fe II $\lambda 4352$	55	3(.05)	0(.00)	0(.00)	3(.05)	0(.00)	49(.89)

Table 4
Object profile classification summary

Object ID (1)	N_{PC}^a (2)	N_{IPC} (3)	N_{DP} (4)	N_E (5)	N_A (6)	N_F (7)	N_{tot}^b (8)	Red abs. (9)	Blue abs. (10)
AB Aur	4	0	0	5	1	16	26	No	Yes

Table 4 — *Continued*

Object ID (1)	N_{PC}^a (2)	N_{IPC} (3)	N_{DP} (4)	N_E (5)	N_A (6)	N_F (7)	N_{tot}^b (8)	Red abs. (9)	Blue abs. (10)
AE Lep [†]	0	0	0	5	0	7	12	No	No
BD+61 154	6	0	0	9	0	10	26	No	Yes
BF Ori	0	2	1	0	8	15	27	Yes	No
BH Cep	1	0	0	0	3	22	26	No	Yes
CQ Tau	0	0	1	2	0	24	27	No	No
DW CMa	5	0	0	7	0	12	25	No	Yes
GSC 04794-08227	0	0	0	6	0	20	26	No	No
HD 141569 [†]	0	0	2	1	0	27	30	No	No
HD 142666	0	1	1	1	0	25	28	Yes	No
HD 163296	1	1	0	3	1	21	27	Yes	Yes
HD 169142	0	0	0	2	0	23	25	No	No
HD 190073	2	0	0	12	0	14	29	No	Yes
HD 203024 [†]	0	0	0	1	0	26	27	No	No
HD 244314	2	0	0	7	0	20	29	No	Yes
HD 244604	2	0	0	5	0	19	26	No	Yes
HD 245185	0	0	1	3	2	20	26	Yes	No
HD 249879	2	0	0	4	0	18	24	No	Yes
HD 250550	2	0	0	4	0	6	12	No	Yes
HD 287823	1	0	0	1	0	24	26	No	Yes
HD 290409	0	0	1	1	0	24	26	No	No
HD 290500	0	0	1	0	0	25	26	No	No
HD 290764	0	0	0	2	0	24	26	No	No
HD 290770	1	0	0	5	0	20	26	No	Yes
HD 34282	0	0	1	0	0	25	26	No	No
HD 35187	0	2	0	1	0	24	27	Yes	No
HD 35929 [†]	0	0	1	1	0	24	26	No	No
HD 36408 [†]	1	0	0	5	0	19	25	No	Yes
HD 37357	2	0	0	1	0	23	26	No	Yes
HD 37411	0	0	1	1	0	10	12	No	No
HD 38120	0	1	1	2	0	8	12	Yes	No
HD 50083 [†]	0	0	3	1	0	21	26	No	No
HK Ori	0	0	2	3	0	21	26	No	No
IL Cep [†]	0	0	2	0	0	24	26	No	No
IP Per	0	0	0	4	0	22	26	No	No
IRAS 05044-0325	0	0	2	1	0	22	25	No	No
IRAS 06071+2925	2	0	0	5	0	18	26	No	Yes
IRAS 07061-0414	0	0	0	0	0	25	25	No	No
IRAS 17481-1415	0	0	0	2	0	18	21	No	No
IRAS 18306-0500	0	0	0	0	0	23	23	No	No
IRAS 18454+0250	0	0	0	1	0	19	20	No	No
LkH α 134	2	0	0	6	0	18	26	No	Yes
LkH α 208	0	0	1	2	0	24	27	No	No
LkH α 233	2	0	0	4	0	17	23	No	Yes
LkH α 257	0	0	2	0	0	20	22	No	No
LkH α 324	0	0	2	0	0	21	23	No	No
LkH α 339	0	0	0	3	0	19	22	No	No
MWC 1080	9	0	0	4	0	10	25	No	Yes
MWC 120	0	3	3	7	0	12	26	Yes	No
MWC 137	0	0	0	13	0	10	24	No	No
MWC 147	0	0	3	3	0	16	22	No	No
MWC 300	0	0	2	12	0	12	26	No	No
MWC 361	0	0	3	1	0	21	26	No	No
MWC 480	6	0	1	1	3	13	25	No	Yes
MWC 610 [†]	0	0	2	0	0	27	29	No	No
MWC 614	0	0	0	2	0	24	26	No	No
MWC 758	2	0	0	4	0	20	26	No	Yes
MWC 778	0	0	2	3	0	8	13	No	No
MWC 863	2	0	0	3	0	20	25	No	Yes
NZ Ser	0	0	0	7	0	13	21	No	No
R Mon	1	0	1	7	0	13	22	No	Yes
RR Tau	0	1	2	3	0	21	27	Yes	No
SV Cep	0	0	1	1	0	23	25	No	No
T Ori	0	1	2	5	0	19	27	Yes	No
UX Ori	0	5	0	3	0	15	23	Yes	No
UY Ori	0	0	1	2	2	7	12	No	Yes
V1185 Tau	1	0	0	2	0	24	27	No	Yes
V1578 Cyg	7	0	0	2	2	14	26	No	Yes
V1685 Cyg	1	1	4	3	0	20	29	Yes	Yes
V1686 Cyg	0	0	2	2	0	16	19	No	No
V1787 Ori	0	0	1	1	0	21	23	No	No
V1818 Ori	0	0	5	1	2	16	24	Yes	No
V346 Ori	0	1	0	0	1	24	26	Yes	No
V351 Ori	0	2	0	0	2	22	26	Yes	No
V361 Cep [†]	0	0	1	3	0	21	26	No	No

Table 4 — *Continued*

Object ID (1)	N_{PC}^a (2)	N_{IPC} (3)	N_{DP} (4)	N_E (5)	N_A (6)	N_F (7)	N_{tot}^b (8)	Red abs. (9)	Blue abs. (10)
V373 Cep	3	0	0	3	0	15	22	No	Yes
V374 Cep	3	0	1	0	2	22	29	No	Yes
V380 Ori	0	0	0	8	0	5	14	No	No
V586 Ori	0	1	1	6	2	16	26	Yes	No
V590 Mon	0	0	2	4	0	20	26	No	No
V599 Ori	0	1	0	2	0	15	18	Yes	No
V718 Sco	0	1	0	0	1	21	23	Yes	No
V791 Mon	2	0	0	6	0	5	13	No	Yes
VV Ser	0	2	3	3	0	17	25	Yes	No
WW Vul	0	2	1	3	2	20	28	Yes	No
XY Per	0	1	1	0	5	18	26	Yes	No
Z CMa	13	0	0	5	1	7	27	No	Yes
Total fraction^c:	0.36	0.23	0.45	0.83	0.22	0.26 ^{+0.05} _{-0.05}	0.37 ^{+0.06} _{-0.05}

^a Total number of line profiles that show the specified morphology.

^b Total number of line profiles examined for each object.

^c Total fraction of objects that display the specified profile or absorption type.

Table 5
Comparison to previous studies

Study (1)	N_{tot} (2)	N_{RA} (3)	% RA (4)	N_{BA} (5)	% BA (6)
Present work	78	20	26 ⁺⁵ ₋₅	29	37 ⁺⁶ ₋₅
FM84	46	2	4 ⁺⁴ ₋₂	16	35 ⁺⁷ ₋₇
HP92	32	2	6 ⁺⁶ ₋₃	11	34 ⁺⁹ ₋₈
R96	18	1	6 ⁺⁸ ₋₃	2	11 ⁺⁹ ₋₅
V03	131	18	15 ⁺⁴ ₋₃

The difference in red-absorption statistics between our study and the others listed in Table 5 is more pronounced. We find that 26% of our objects show red-shifted absorption in at least one line while the studies of FM84, HP92, and R96 show roughly a 4–6% occurrence. The discrepancy is easily explained for our study versus those of FM84 and R96: the occurrence of red-shifted absorption at H α in our study is \sim 6%, comparable to that found by FM84 and R96 both of which primarily examine H α . FM84 also examine the Na I D lines but both their sample and ours show a negligible occurrence of red-shifted absorption in those lines.

The discrepancy with HP92 is harder to explain. A large percentage (15%) of our objects show red-shifted absorption at He I λ 5876. The rest of the red-shifted absorption detections result mainly from H α , H β , and Ca II IRT lines. HP92 also examine these lines but they detect red-shifted absorption in only 2 out of 32 objects, a detection rate of \sim 6%. This might be explained by the fact that HP92 only observe 6 objects at He I λ 5876 and thus, to obtain a detection rate at λ 5876 similar to that of our sample, they would, on average, detect red-shifted absorption in \sim 1 object, which they do. The non-detections in the other lines is more puzzling but may be accounted for by the lower resolution of their observations (11–85 km s⁻¹). These medium-resolution observations may mask weak red-shifted absorption signatures. We note that the red-shifted absorptions observed

at H α and H β in our sample tend to appear as deeper absorptions superimposed on a photospheric absorption core. However, when these lines are carefully compared to a rotationally broadened standard it is clear that the red-shifted absorptions are non-photospheric and that the profile morphology is inverse P-Cygni. It is not clear that HP92 compare their objects to photospheric standards. If not, this may also contribute to the discrepancy.

By comparison to the studies listed above, our analysis demonstrates the necessity of large sample, high-spectral resolution studies of outflow and inflow diagnostics in HAEBES in order to gather accurate statistics of mass flows around these objects. The H β diagnostic shows the largest percentage of P-Cygni profiles, although other lines (e.g. H α , H γ , Fe I 4924) also show non-negligible P-Cygni detection fractions. The He I λ 5876 line is by far the most sensitive line for detecting inverse P-Cygni morphologies. This is not surprising since the He I λ 10830 line is also a very efficient diagnostic for detecting mass flows (Edwards et al. 2006; Cauley & Johns-Krull 2014) and the λ 5876 transition lies immediately above the upper energy level of the λ 10830 transition, preceding λ 10830 in a recombination cascade sequence. The Na I D lines are also relatively sensitive to outflows in HAEBES, although the lines more frequently display pure emission profiles.

5.4. Comparison to He I λ 10830 data

The line profile statistics (Table 6) for both inflows and outflows from our optical data set are similar to those from the He I λ 10830 data set, although the fractions are higher in the He I λ 10830 sample.

We use contingency tests to compare the fractions of red and blue-shifted absorption between the two studies. A contingency test of the measured fraction of a characteristic in two groups gives the probability that the null hypothesis is true, i.e. that the intrinsic fraction is the same in both groups (Feigelson & Babu 2012). This probability is referred to here as the p -value. A high p -value indicates a high probability of having obtained the difference in the measured fractions by chance, i.e. the null hypothesis cannot be ruled out; a low p -value indicates a low probability that the difference in the measured fractions was obtained accidentally, i.e. the difference is real and the null hypothesis can probably be ruled out. A contingency test comparing the He I λ 10830 sample to

the optical sample shows that neither the blue-shifted ($p=0.85$) nor the red-shifted ($p\sim 1.0$) absorption incidences are significantly different.

Table 6
Comparison to He I $\lambda 10830$ HAEBE statistics

	Optical data (1)	He I $\lambda 10830$ data (2)
N_{tot}	78	48
Red-shifted abs.	26% $^{+5}_{-5}$	27% $^{+7}_{-6}$
Blue-shifted abs.	37% $^{+6}_{-5}$	40% $^{+7}_{-7}$

Although the overall morphology statistics are similar between the optical and He I $\lambda 10830$ data, the He I $\lambda 10830$ line is much more efficient at tracing mass flows around HAEBES than any *single* optical diagnostic. In addition, He I $\lambda 10830$ is generally less contaminated by sources other than nearby circumstellar material due to the high excitation temperatures needed to populate the lower energy level ($\sim 20,000$ K; Dupree et al. 2005). This is not the case for other popular diagnostics such as H α , H β , and the Na I D lines which can frequently display strong emission signatures from chromospheres, nebular background, and interstellar absorption in the case of Na I D. The tendency of the He I $\lambda 10830$ line to remain in its lower energy level until a photon is absorbed accounts for the large opacity needed to generate the blue-shifted absorption commonly seen in the data from Paper I.

Figure 9 compares the maximum absorption velocities of He I $\lambda 10830$ and H α or H β for objects that display blue-shifted absorption in both He I $\lambda 10830$ and H α (red diamonds) and H β (blue crosses). This figure shows that He I $\lambda 10830$ traces approximately the same outflow velocities as H α and H β , although the velocities in H β are generally smaller when compared to He I $\lambda 10830$. This could be due to the larger optical depth of He I $\lambda 10830$ and H α relative to H β , allowing photons to be absorbed up to larger fractions of the terminal wind velocity. The number of objects with both optical and He I $\lambda 10830$ data that also show blue-shifted absorption is small and thus it is not possible to make a strong case for choosing one of the optical diagnostics over He I $\lambda 10830$ based on a velocity comparison. Each line appears to trace similar material in the wind. Thus for future studies concerned with detecting the presence of outflows and accretion around HAEBES, He I $\lambda 10830$ could serve as a primary diagnostic due to its high efficiency in detecting mass flows. In addition, it is relatively free of photospheric and interstellar contaminants making the circumstellar nature of the line morphologies unambiguous. In terms of mass flow statistics and outflow velocities, it appears that optical data does not provide any additional information over that provided by the He I $\lambda 10830$ line.

5.5. Comparison to CTTs

To our knowledge, the study performed by Alencar & Basri (2000, hereafter AB00) is the only current high-resolution, moderate sample size investigation of CTTs that examines many different spectral line diagnostics. We take the statistics from AB00 to be representative of

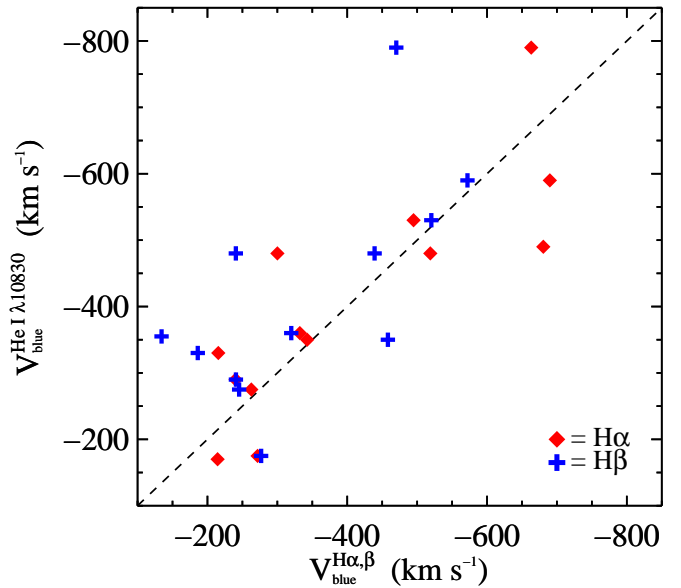


Figure 9. Maximum blue-shifted absorption velocities seen in He I $\lambda 10830$ vs H α and H β for objects with blue shifted absorption at both He I $\lambda 10830$ and either H α or H β . The He I $\lambda 10830$ and the Balmer lines generally trace the same velocity of outflowing material, although there is significant scatter. The H β line velocities match the He I $\lambda 10830$ velocities less well than the H α velocities. This may be an optical depth effect: the optical depth at H β may simply be too low to trace the same wind extent as He I $\lambda 10830$ and H α , resulting, in general, in smaller observed velocities at H β . Note that the data for the optical lines and the He I $\lambda 10830$ lines are not simultaneous.

CTTs in general. AB00 examine the following accretion and outflow diagnostics: H α , H β , H γ , H δ , He I $\lambda 5876$, Na I D, Ca II K, Ca II $\lambda 8662$, Ca II $\lambda 8498$, Fe I $\lambda 6192$, $\lambda 5497$, and Fe II $\lambda 4924$ and $\lambda 4352$. Our study is well suited for comparison with AB00 since we examine all of these except for Fe I $\lambda 6192$. The resolving power of their observations ($R \sim 48,000$) is also similar to ours increasing the chance that no weak features will be missed in one data set but not in the other. We will also compare certain profile statistics from our sample to those of Beristain et al. (2001) and Batalha et al. (1996), studies which analyzed a smaller number of mass flow diagnostics in similar sample sizes of CTTs to that of AB00.

AB00 find high fractions of both red-shifted absorption (12 objects, 40% $^{+9}_{-8}$) and blue-shifted absorption (24 objects, 80% $^{+6}_{-8}$) in at least one line for the CTTs in their sample. Our sample displays much lower incidences of both red and blue-shifted absorption: 26% and 37%, respectively. Contingency tests comparing our study to the of Alencar & Basri (2000) are shown in Table 7. The red-shifted absorption comparison between our final sample and that of AB00 suggests a marginal difference ($p=0.16$) in the incidence of red-shifted absorption. The blue-shifted absorption statistics are significantly different for both sample comparisons, with $p < 0.001$.

Table 7
Optical contingency table results

Feature	Groups	p -value
Red absorption	HAEBES vs CTTSs	0.160
Blue absorption	HAEBES vs CTTSs	9×10^{-4}

In addition to the total mass flow statistics, there are differences in the absorption statistics in the lines that are common to both our study and that of [AB00](#). This comparison is presented in [Table 8](#) and is shown graphically in [Figure 10](#). The most common line displaying blue-shifted absorption in their data is $H\alpha$ followed by $H\beta$, $H\gamma$, $H\delta$ and the Na I D lines. A similar trend is observed in our data except that $H\beta$ shows a slightly higher incidence of blue-shifted absorption than $H\alpha$. The most common red-shifted absorptions features appear at He I $\lambda 5876$ and Na I D in their sample. The highest red-shifted absorption occurrence in our data is also at He I $\lambda 5876$. However, we observe only 1 object with red-shifted absorption at Na I D. We find a small incidence of inverse P-Cygni profiles in $H\alpha$ and $H\beta$ (6% and 5%, respectively) while [AB00](#) observe a larger incidence of red-shifted absorption components at $H\alpha$ (23%) and $H\beta$ (23%). [AB00](#) find Fe II $\lambda 4924$ in emission in 40% of their sample. Our data show Fe II $\lambda 4924$ emission in only 9% of the sample. We also observe both blue and red-shifted absorption at Fe II $\lambda 4352$ in a non-negligible fraction (13%) of our sample. [AB00](#) do not fit for the absorption components at Fe II $\lambda 4352$, likely due to strong nearby photospheric features. By comparing the CTTS $\lambda 4352$ lines in their sample to that of V410 Tau, a WTTS also

from their sample, we searched for red and blue-shifted absorption in the line. We find no profiles that are not consistent with purely photospheric absorption. Thus we estimate the mass flow incidence in this line to be ~ 0 in the [AB00](#) CTTS sample.

The largest incidence differences between our sample and [AB00](#), outside of the Balmer lines, occur in the Na I D lines, He I $\lambda 5876$, Fe I $\lambda 5498$, and Fe II $\lambda 4924$. At He I $\lambda 5876$ we find a higher occurrence of red-shifted absorption (15%) than [AB00](#) (10%). Our observed fraction of He I $\lambda 5876$ red-shifted absorption is more similar to that found by [Beristain et al. \(2001\)](#) (16%) for a sample of 31 CTTSs. We find significantly lower fractions of red-shifted absorption in both Na I D lines (8%) compared to [AB00](#) (27%). We find a red-shifted absorption fraction of 8% at Fe II $\lambda 4924$. [AB00](#) do not observe any red-shifted absorption at Fe II $\lambda 4924$. Similar discrepancies are observed in the blue-shifted absorption statistics. At Fe I $\lambda 5498$, we find no evidence of blue-shifted absorption in *any* objects while [AB00](#) report a detected fraction of 60%. Our detected blue-shifted absorption fraction at Na I D ($\sim 10\%$) is also much lower than [AB00](#), 's (40%). Finally, the blue and red-shifted absorption fractions at $H\alpha$, $H\beta$, $H\gamma$, and $H\delta$ are significantly higher in [AB00](#)'s sample of CTTSs than in our HAEBE sample.

Although we do not focus on the pure emission profiles, we note that our detected fraction of emission at He I $\lambda 5876$ is low (14%) compared to that of [Beristain et al. \(2001\)](#) who detect emission in 100% of their 31 CTTSs. In §6 we will comment on possible causes for this differing line profile statistic. The possible physical causes of the absorption statistics detailed above will be outlined in the next section.

Table 8
Comparison to line absorption statistics from [Alencar & Basri \(2000\)](#)

		$H\alpha$	$H\beta$	$H\gamma$	$H\delta$	He I $\lambda 5876$	Na I $\lambda 5889$	Na I $\lambda 5896$	Ca II $\lambda 8662$	Ca II $\lambda 8498$	Ca II $\lambda 3969$	Fe I $\lambda 5498$	Fe II $\lambda 4924$	Fe II $\lambda 4352$
		(1)	(2)	(3)	(4)	(5)	(6)	(7)	(8)	(9)	(10)	(11)	(12)	(13)
AB00	N_{RA}	9	8	8	8	3	8	8	4	1	1	0	0	0
	% RA	30	31	31	35	10	27	27	13	3	4	0	0	0
	N_{BA}	23	14	8	6	0	12	12	0	1	2	18	0	0
	% BA	77	54	31	26	0	40	40	0	3	7	60	0	0
This study	N_{RA}	5	7	3	3	12	6	6	2	1	0	0	5	0
	% RA	6	9	5	6	15	8	8	3	4	0	0	8	0
	N_{BA}	21	24	12	7	1	8	7	2	2	1	0	7	3
	% BA	24	32	20	14	1	10	9	3	8	2	0	11	5

6. DISCUSSION

The optical line statistics presented in §5 indicate that there are differences in the characteristics of, and/or the physical mechanisms producing, the mass flows in CTTSs vs HAEBES. Below we discuss possible scenarios capable of producing the trends and differences seen in the measured statistics.

6.1. Fe II: Higher ionization states tracing mass flows in HAEBES

[Table 8](#) shows clear evidence that HAEBES, in general, show significantly more mass flow activity in the

Fe II lines than CTTS indicating an absorbing region that is hotter or is subject to higher amounts of ionizing radiation. Fe I $\lambda 5498$ shows a 60% incidence of blue-shifted absorption in [AB00](#)'s sample but is not detected in absorption in any of our HAEBES. The reverse is true for the Fe II $\lambda 4924$ and $\lambda 4352$ lines: we see non-zero fractions of both lines exhibiting blue-shifted absorption while [AB00](#) do not detect absorption in either of these lines in any objects. All of the objects in which we detect blue-shifted absorption in Fe II are B-type or early A-type objects. This behavior was also noted by [Hamann & Persson \(1992\)](#) concerning the relative strengths of Fe I and Fe II emission lines in HAEBES versus CTTSs. The first ionization potential of Fe is 7.9 eV which corre-

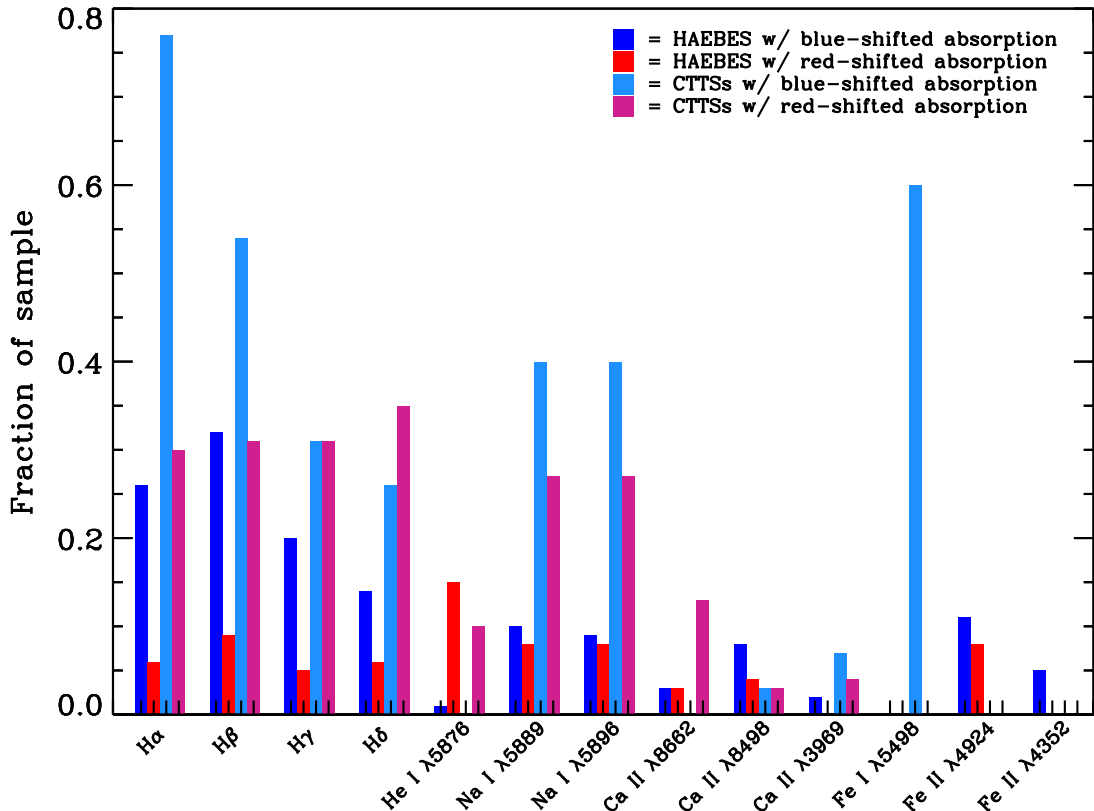


Figure 10. Line-by-line mass flow fraction comparison of CTTS and HAEBE samples. The fractions are listed as percentages in Table 8. The CTTS data is from AB00. The CTTSs, in general, show a higher incidence of both blue and red-shifted absorption in most line diagnostics compared to HAEBES. The exceptions are at He I λ 5876 and the Fe II lines.

sponds to a wavelength of 1570 Å. The ionizing radiation flux for a 10,000 K blackbody, a similar temperature to T_{eff} for an A0 star, is $\sim 10^6$ times higher at 1570 Å than for a 3,800 K blackbody, a typical T_{eff} for a CTTS of spectral type M0. In addition, CTTSs display large UV excess fluxes due to accretion which can be 10^4 – 10^5 times higher than the stellar photosphere at typical temperatures used to model the excess continuum. Thus the actual flux ratio at 1570 Å is likely much lower than 10^6 but still favors HAEBES over CTTSs. The larger number of ionizing photons emitted by B and early A stars compared to CTTSs could account for the observed disparities in the Fe II line profile statistics observed here.

This trend also holds for another low ionization potential metal, Na I, which is ionized by photons with energies higher than 5.1 eV, or $\lambda \lesssim 2431$ Å. The overall mass flow incidence in our sample is much lower at Na I D than in AB00’s sample. However, we do observe Na I outflow signatures in a majority of our objects that also display blue-shifted absorption at Fe II, indicating that significant amounts of neutral material are simultaneously present in these outflows. Although it is unclear to what extent the temperature of the outflow determines the ionization state of the wind compared to the ionizing flux from the star, Na I is likely not present in the regions of the outflow being sampled by Fe II. The observed statistics for Ca II are not significant enough to warrant a comparison to those from AB00. It appears that the

differences in Fe I and Fe II and Na I morphology statistics between HAEBES and CTTSs suggest more highly ionized environments around HAEBES, likely due to the higher number of ionizing photons emitted by HAEBES.

6.2. Infall velocities

In Paper I we showed that, on average, the maximum red-shifted absorption velocities in HAEBES are smaller fractions of the stellar escape velocity than in CTTSs (see Figures 5 and 6 from Paper I). The comparison in Paper I was performed using only the line velocities measured from He I λ 10830 data. Here we present the same comparison in Figure 11 but incorporating all of the optical diagnostics displaying red-shifted absorption for each object. For HAEBES that show red-shifted absorption in more than one diagnostic, their average value is used. We note that, as in Paper I, Figure 11 is identical in format to Figure 5 from Fischer et al. (2008) in order to facilitate easy comparison with the red-shifted He I λ 10830 absorption velocities presented in that study. The diagonal lines mark the velocity ratios that correspond to the infall distance from the stellar surface, given in stellar radii, marked above each line. In other words, the dotted line shows the maximum free-fall velocity that can be obtained if infall begins at the specified distance from the star. We estimate the red-shifted absorption velocities of 13 CTTSs from the published optical profiles of Edwards et al. (1994). Edwards et al. (1994) observed

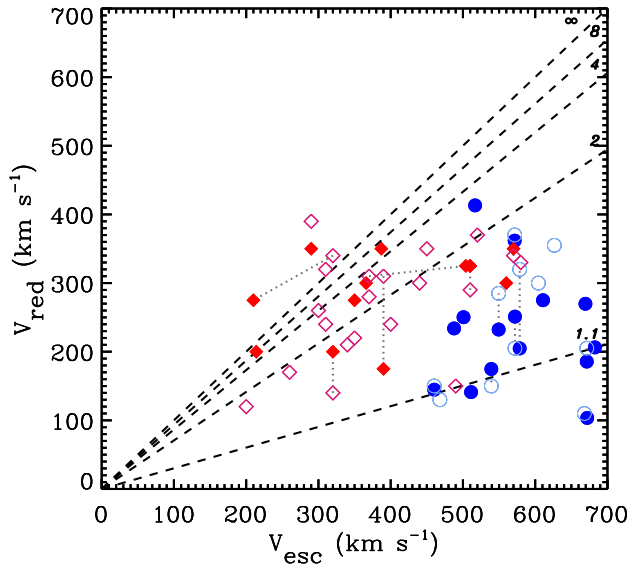


Figure 11. Observed maximum red-shifted absorption velocities versus stellar escape velocity for the HAEBES (filled blue circles) from this study and CTTs from [Edwards et al. \(1994\)](#) (filled red diamonds). The unfilled plot symbols are the HAEBE (light blue) and CTTs (light red) objects from the He I $\lambda 10830$ samples of [Paper I](#) and [Fischer et al. \(2008\)](#), respectively. Objects common to both the optical and He I $\lambda 10830$ samples are connected by a dotted line. The dashed lines show, for a given V_{esc} , the maximum velocity obtained if infall begins from the distance labeled next to the line (in stellar radii). The HAEBES, on average, show maximum red-shifted absorption velocities that are smaller fractions of their stellar escape velocities, indicating that the infalling material originates closer to the stellar surface.

Balmer line profiles as well as Na I D and He $\lambda 5876$. Most of the red-shifted absorption profiles in our sample are not seen in the same lines so the comparison should not be subject to lines tracing mass flows with significantly different physical conditions.

In [Figure 11](#) the CTTs are plotted as solid red diamonds; the HAEBES are represented by the filled blue circles. For comparison we have overplotted the HAEBES He I $\lambda 10830$ velocities from [Paper I](#) as light blue unfilled circles and the He I $\lambda 10830$ CTTs velocities from [Fischer et al. \(2008\)](#) as unfilled light red diamonds. Objects that are common to both the optical and He I $\lambda 10830$ samples have their velocities, as measured at He I $\lambda 10830$ and in the optical diagnostics, connected by a dotted line². The mean velocity ratio (V_{red}/V_{esc}) for the HAEBE sample is 0.40; for the CTTs it is 0.78. A two-sided KS-test performed on the sample returns a p -value of 2.2×10^{-5} indicating a significant difference between the two populations.

In order to test the effect of uncertainties in determining V_{esc} on the KS statistic, we generated ten thousand random velocity distributions and performed a KS test on each one. We follow the same procedure for assigning uncertainties to the stellar mass and radius (50% and 25%, respectively) as performed in [Paper I](#). In addition, we let the measured red-shifted absorption velocity vary by 50%. This provides some accounting of accretion variability. The result of the KS-tests is shown in the bottom

² Two CTTs are plotted with two different estimates of their escape velocities due to different M_* and R_* estimates from the studies that the spectral line velocities are taken from.

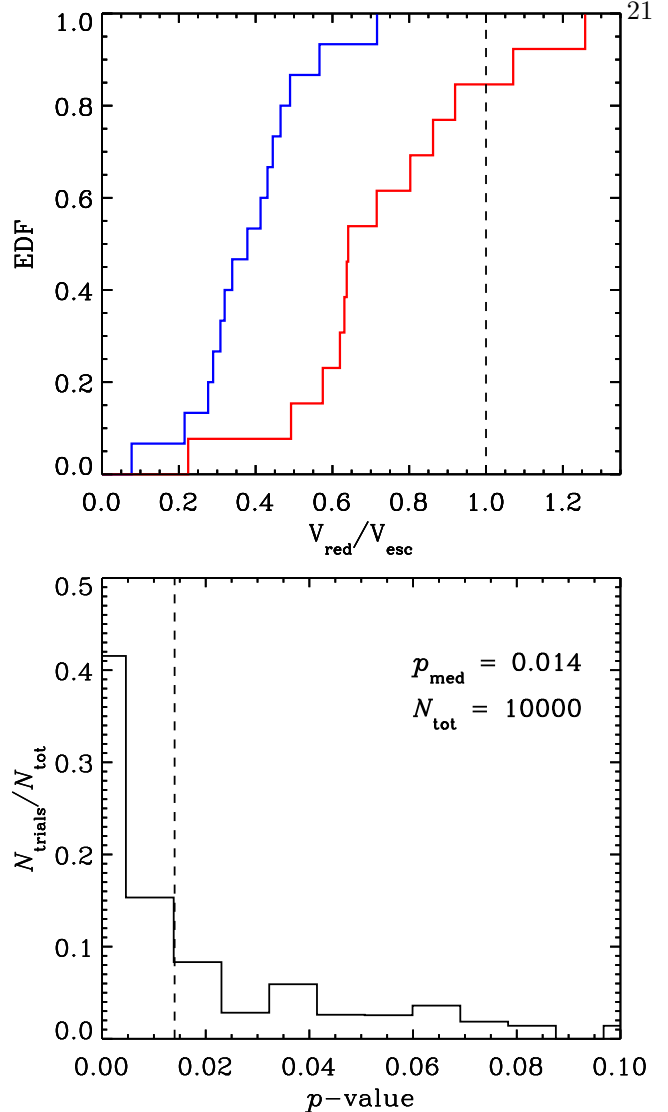


Figure 12. Histogram showing the distribution of KS test p -values (bin width of 0.0005) for ten thousand trials (bottom panel) and EDFs for the HAEBE and CTTs samples (top panel). The median value of p_{KS} is marked by the vertical dashed line in the bottom panel. In the top panel, the HAEBE EDF is shown in blue; the CTTs EDF is shown in red. A majority of the tests (74%) return $p < 0.05$ indicating a significant difference between the two EDFs.

panel of [Figure 12](#) where the median p -value is seen to be ~ 0.014 . The empirical distribution function (EDF) for each sample is shown in the upper panel. For each of the trials each object is assigned a random value within the limits of the uncertainty in the object's escape velocity and red-shifted absorption velocity. The low p -values suggest a real difference in the distributions which in turn indicates that accretion flows in HAEBES begin deeper in the system's gravitational potential, i.e. closer to the star. This supports the similar result found in [Paper I](#), although the p -values are, on average, higher in the optical case due to the red-shifted absorption velocity being allowed to vary in the simulation.

[Figure 11](#) and [Figure 12](#) provide additional support for our suggestion in [Paper I](#) that HAEBES have smaller magnetospheres than CTTs. The evidence in the optical is perhaps even more convincing due to the larger number of red-shifted absorption lines used in the com-

parison, although there is a large spread in the measured line absorption velocities for some individual objects. However, the lack of large p -values in our KS test simulation indicates that the velocity ratio difference between HAEBES and CTTSs is independent of the particular line velocity chosen for the comparison. The statistical tests also support the idea that the red-shifted absorption in HAEBES originates deeper within the gravitational potential of the central star. If the relative distances are similar at which the magnetospheres in HAEBES and CTTSs are dominating the kinematics of the accretion flow, the velocity ratios of the HAEBE and CTTS samples should be comparable. Since they are not, there must be some difference in the formation mechanisms of the absorption signatures. We attribute this difference to smaller magnetospheres in HAEBES compared to CTTSs. We note that smaller corotation radii, and thus smaller magnetospheres, are suggested for most HAEBES compared to CTTSs due to their large $v\sin i$ values (see §2 of Paper I; Muzerolle et al. 2004). Thus, this result is expected from magnetospheric accretion physics.

6.3. H Ae stars vs H Be stars

In Paper I we demonstrated the lack of red-shifted absorption at He I $\lambda 10830$ in HBe stars (Figure 7 of Paper I). This same trend holds for our larger optical sample. This is shown in Figure 13, which plots the difference between the blue ($v < 0$) and red ($v > 0$) line equivalent widths versus T_{eff} , for the objects with at least one profile displaying evidence of blue or red-shifted absorption. If an object shows more than one profile in absorption, we average the equivalent width difference. The equivalent width difference is essentially a measure of profile type: red-shifted absorption results in a negative equivalent width difference while blue-shifted absorption results in a positive equivalent width difference. Objects in each quadrant are color-coded for clarity. There is an absence of objects in the upper-left quadrant. Although V1818 Ori shows evidence of red-shifted absorption in the Na I D lines, we do not calculate an equivalent width for either line due to the strong interstellar absorption features superimposed on the line. Thus there are only 3 HBe objects with red-shifted absorption shown in Figure 13 and they all lie very close to the vertical dashed line. The IPC and red absorption He I $\lambda 5876$ profiles generally have small equivalent width differences ($0.0 \text{ \AA} > W_b - W_r > -2.0 \text{ \AA}$) and comprise most of the red-shifted absorption objects (red crosses and magenta right-facing triangles).

This result is also born out in the overall profile statistics: 15 of the 19 red-shifted absorption objects are H Ae stars; 4 are H Be stars, with 2 of those having spectral types of B9. There are 45 H Ae stars in the final sample and 33 H Be stars. A contingency test comparing H Ae and H Be red-shifted absorption returns $p=0.04$ providing support for a real difference in the morphology statistics. A test comparing the blue-shifted absorption reveals no difference between H Ae and H Be objects ($p=0.48$). A similar trend is seen in the He I $\lambda 10830$ data but the larger optical sample has added significance to the red-shifted absorption comparison.

The similarity in the optical and He I $\lambda 10830$ H Ae versus H Be comparisons suggests that the conclusions

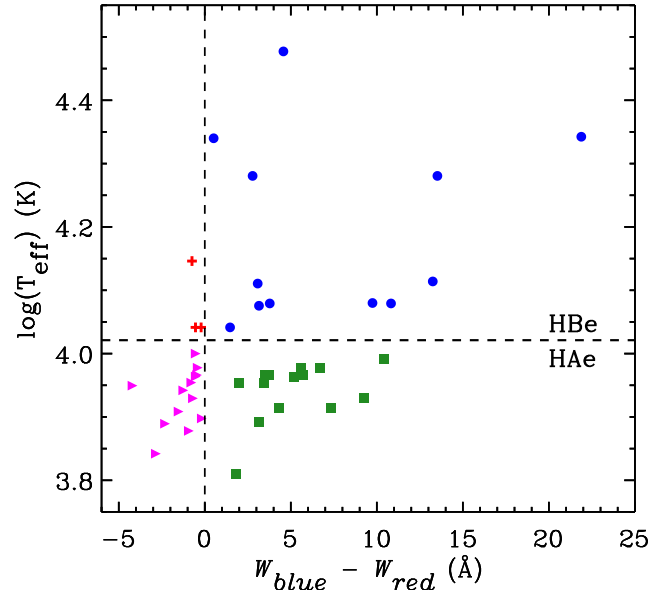


Figure 13. The T_{eff} vs blue equivalent width minus red equivalent width for all of the objects in our sample that have absorption profiles. Objects with more than one line in a quadrant are shown using the average of the equivalent width differences for those lines. Colors are used for clarity in distinguishing quadrants. The trend found for the He I $\lambda 10830$ data from Paper I holds for the optical sample: there is a lack of red-shifted absorption profiles in HBe stars. The strongest blue-shifted absorption profiles are found in the HBe group.

reached in Paper I are not altered by the analysis presented here. H Ae stars exhibit red-shifted absorption more frequently than H Be stars indicating that mass infall, most likely magnetically channeled, is more common in H Ae stars. Outflows seem to be present in similar fractions of H Ae and H Be objects suggesting that the wind mechanism is equally as efficient in both groups of objects.

6.4. Simultaneous blue and red-shifted absorption and accretion driven outflows

In Paper I we noted the lack of simultaneous blue and red-shifted absorption in the He I $\lambda 10830$ profiles. To clarify, simultaneous absorption signatures in the current, optical context refer to detected absorption in *any* diagnostics from the same exposure, or exposures taken very close in time to one another. This includes simultaneous red and blue-shifted detections in the same line, such as that seen in He I $\lambda 10830$ for the CTTSs from Edwards et al. (2006), or detections in two different lines as seen in Alencar & Basri (2000). This lack of simultaneous absorption contrasted sharply with the large detected fraction of simultaneous absorption signatures in CTTSs presented by Edwards et al. (2006).

The optical data continues this trend: we observe only 1 object (HD 163296) that shows clear red and blue-shifted absorptions signatures in at least one line from the same exposure. Based on the published centroid velocities of the detected absorption features from AB00, we count 17 out of 30 CTTSs, or 57%, showing red and blue-shifted absorption in at least one line from nearly simultaneous exposures. The lack of simultaneous absorption features observed in our optical sample supports the arguments presented in Paper I, namely that accre-

tion driven outflows in HAEBES may be more difficult to produce. The strong optical outflow signatures observed in both HAe and HBe objects that do not also exhibit red-shifted absorption, combined with the conclusion from [Paper I](#) that the He I $\lambda 10830$ PC morphologies are likely accretion-driven, suggests that accretion in some HAEBES may proceed through a non-magnetic mechanism such as a boundary layer. This would explain the relative lack of simultaneous red and blue-shifted absorption signatures in HAEBES compared to CTTs.

It is still unclear whether or not the accretion flows detected in the red-shifted absorption objects can drive outflows. Outflow signatures in these objects are not observed (except for HD 163296) suggesting that if the accretion is related to driving outflows, the outflow signatures are too weak to be detected or are launched in a geometry that requires a specific viewing angle to observe (e.g. a highly collimated jet emerging from the polar region). This seems unlikely since these simultaneous signatures are almost entirely absent from our sample, suggesting that they are present in very few objects. Indeed, jets have been detected in a relatively fewer number of HAEBES (e.g. [Grady et al. 2004](#); [Ellerbroek et al. 2014](#)) compared to CTTs hinting that they do not form as efficiently in HAEBES.

One potential explanation is that, in general, the accreting material as traced by red-shifted absorption is not energetic enough to provide the energy necessary to drive an outflow. Support for this idea is seen in [Figure 11](#) from this study and [Figure 5](#) from [Paper I](#) where the red-shifted absorption velocities of HAEBES are found to be smaller fractions of their stellar escape velocities. We also find support for this scenario in [Figure 7](#) from [Paper I](#) which demonstrates the relative lack of objects with low accretion rates that also exhibit blue-shifted absorption profiles. We note that this distinction is not clear in our optical data, i.e. the separation of profile type with accretion rate is not distinct. We have fewer estimates of \dot{M} in hand, however, for the red-shifted absorption objects from the optical sample and thus the comparison is less significant. This could be improved and further tested by obtaining simultaneous line profile morphologies and accretion rate estimates for a large sample of HAEBES.

The idea of accretion powered stellar winds was first proposed for CTTs by [Matt & Pudritz \(2005\)](#). They suggest that a portion of the deposited accretion energy will heat the corona (via conduction or magnetosonic wave dissipation) and assist in launching stellar winds. While it is unclear whether or not this process is occurring in CTTs, magnetically channeled accretion, involving smaller magnetospheres in HAEBES compared to CTTs, will provide a smaller fraction of the necessary energy for launching an outflow from the stellar surface of HAEBES than from the surface of CTTs. Since the outflows observed in CTTs are generally accepted to be driven largely by accretion (e.g. [Hartigan et al. 1995](#); [Edwards et al. 2006](#)), the amount of energy deposited by the accretion flow onto the stellar surface could strongly influence the strength of the outflow. For HAEBES, if we imagine that all of the kinetic energy of the accretion flow is converted into kinetic energy in a wind driven from very near the stellar surface (i.e. a

stellar wind), these outflows will be incapable of escaping the gravitational potential of the star due to the small (~ 0.5 ; [Figure 11](#)) fractions of the stellar escape velocity that the accretion flows attain during their infall. Obviously this is an ideal scenario, but the energy budget argument holds if a large portion of the energy in the wind is provided by the accretion flow, which it seems to be in CTTs. To summarize, the lower infall velocities relative to the stellar escape velocities in HAEBES may indicate that these accretion flows cannot efficiently drive mass outflows from the stellar surface.

If magnetically controlled mass infall in HAEBES is incapable of driving outflows, another form of accretion may be partly responsible for driving the outflows from objects with large \dot{M} . We suggested in [Paper I](#) that boundary layer accretion in HAEBES could provide the necessary energy, although it is unclear exactly how the energy is transferred to the outflow. One possible scenario discussed in [Paper I](#) for launching outflows from the boundary layer is the [Shu et al. \(1988\)](#) X-celerator mechanism. The high $v \sin i$ values of HAEBES are ideal for producing this type of outflow. Better \dot{M} estimates for a larger number of HAEBES will help elucidate the relationship between profile type and the role of the accreting material in producing the outflow signatures.

6.5. He I $\lambda 5876$ emission lines

[Beristain et al. \(2001\)](#) examine the He I $\lambda 5876$ in a sample of 31 CTTs. They find an emission component (broad, narrow, or both) in all of the objects in their sample. They interpret the broad component emission as arising in a hot wind as well as in the accretion flow onto the star. The narrow emission component is interpreted as forming in the post-shock gas at the base of an accretion column at the surface of the star. Our sample contains 13 HAEBES that display emission profiles at He I $\lambda 5876$. None of these objects show the narrow component that is commonly seen in CTTs, as well as WTTs. This may be due to the much higher average $v \sin i$ values of HAEBES compared to CTTs. However, 11 of the 13 objects show broad emission profiles similar in width to those observed by [Beristain et al. \(2001\)](#) and 8 objects show unambiguous blue-shifted absorption in a separate but simultaneous diagnostic. Of these 8 objects, five show unambiguous evidence of mass outflow at He I $\lambda 10830$, although these observations are not simultaneous to the He I $\lambda 5876$ observations. Due to the prevalence of blue-shifted absorption observed in the He I $\lambda 5876$ emission objects, our data supports the suggestion by [Beristain et al. \(2001\)](#) that the broad He I $\lambda 5876$ emission component may partly arise in a hot wind near the star.

7. SUMMARY AND CONCLUSIONS

We have presented a large sample census of mass flows around Herbig Ae/Be stars using a wide variety of mass flow diagnostics and determined the fraction of objects that display unambiguous (i.e. red and blue-shifted absorption) mass flow signatures. We find that the Na I D interstellar absorption line centers are good approximations, to within $8.1^{+3.6}_{-3.6}$ km s⁻¹, to the center-of-mass radial velocity in most HAEBE systems, confirming the conclusion reached by [Finkenzeller & Jankovics \(1984\)](#).

Of the 78 HAEBES included in the final analysis, $26\%_{-5}^{+5}$ show direct signs of mass infall and $37\%_{-5}^{+6}$ show direct evidence of mass outflow. These percentages are very similar to those found in [Paper I](#) using the He I $\lambda 10830$ line.

Overall, the optical data reinforce the conclusions outlined in [Paper I](#). More specifically, we find lower rates of both red and blue-shifted absorption for HAEBES than is observed for CTTs, suggesting that, in general, the innermost environments of HAEBES are not simply scaled analogues of CTTs. Similar to the He I $\lambda 10830$ data, the HAEBE optical lines show maximum red-shifted absorption velocities that are smaller fractions of the stellar escape velocities than is found for CTTs. This adds support to the argument presented in [Paper I](#) concerning the smaller size of HAEBE magnetospheres compared to those of CTTs. This has implications for the ability of HAEBE accretion flows to power strong winds: less energetic funnel flows provide less of the required energy for launching outflows. This is supported by the lack of simultaneous blue and red-shifted absorption signatures seen in both the optical sample and the He I $\lambda 10830$ sample from [Paper I](#). This contrasts with CTTs for which the accretion process is believed to be the main energy source for outflows.

We also find a significant difference between the occurrence of red-shifted absorption in H Ae stars compared to H Be stars; both groups appear to exhibit outflow signatures at a similar rate. This suggests that H Be stars accrete material from their disks differently than H Ae stars, perhaps through a boundary layer instead of along magnetic field lines. The prominence of blue-shifted absorption in accreting objects in both subgroups suggests that the outflows in HAEBES are accretion driven. However, the lack of simultaneous red and blue-shifted absorption in all but one HAEBE (HD 163296) indicates that whatever geometry is producing the absorption signature is not capable of producing the opposite absorption signature. In other words, boundary layer accretion, which should not produce red-shifted absorption, may be capable of driving strong outflows which results in observed blue-shifted absorption; magnetically controlled accretion from a small magnetosphere produces red-shifted absorption but is perhaps not energetic enough to drive outflows from the stellar surface, resulting in the lack of simultaneous red-shifted absorption in these profiles. Due to the observed statistics, this suggests a general transition from magnetically controlled accretion in H Ae stars to boundary layer accretion in H Be stars.

We thank the McDonald Observatory staff in West Texas for their hospitality during the observing runs for this research. P. W. C. especially thanks David Doss for his help, without which the collection of some of this data would not have been possible. P. W. C. would also like to acknowledge Pat Hartigan for his comments and discussion throughout this project. We thank the referee for their helpful comments which improved the quality of this manuscript. This research has made use of the SIMBAD database and the NASA Astrophysics Data System. We acknowledge partial support for this research from the NSF through grant 1212122, from NASA Astrophysics Data Analysis Program through

grant NNX13AF09G, and from Space Telescope Science Institute through grant HST-60-12996.001, all made to Rice University.

REFERENCES

- Acke, B., & van den Ancker, M. E. 2004, *A&A*, 426, 151 [3]
 Acke, B., van den Ancker, M. E., & Dullemond, C. P. 2005, *A&A*, 436, 209 [3]
 Alecian, E., et al. 2013, *MNRAS*, 429, 1001 [1, 3, 3]
 Alencar, S. H. P., & Basri, G. 2000, *AJ*, 119, 1881 [5.5, 5.5, 5.5, 8, 6.1, 10, 6.4]
 Alonso-Albi, T., et al. 2009, *A&A*, 117, 136 [3]
 Bagnoli, T., et al. 2010, *ApJL*, 724, L5 [3]
 Batalha, C. C., Stout-Batalha, N. M., Basri, G., & Terra, M. A. O. 1996, *ApJSS*, 103, 211 [5.5]
 Beristain, G., Edwards, S., & Kwan, J. 2001, *ApJ*, 551, 1037 [5.5, 5.5, 6.5]
 350
 Böhm, T., & Catala, C. 1994, *A&A*, 290, 167 [1]
 Böhm, T., & Catala, C. 1995, *A&A*, 301, 155 [1]
 Bossier, J., et al. 2011, *A&A*, 531, A50 [3]
 Carmona, A., van den Ancker, M. E., Audard, M., Henning, Th., Setiawan, J., & Rodmann, J. 2010, *A&A*, 517, A67 [3]
 Caratti o Garatti, A., et al. 2012, *A&A*, 538 A64 [3]
 Catala, C., Böhm, T., Donati, J.-F., & Semel, M. 1993, *A&A*, 278, 187 [1]
 Cauley, P. W., & Johns-Krull, C. M. 2014, *ApJ*, 797, 112 [1, 5.3, 5.4, 6.2, 11, 6.2, 6.3, 13, 6.3, 6.4, 7]
 Chen, L., et al. 2012, *A&A*, 541, A104 [3]
 Corporon, P., & Lagrange, A.-M. 1999, *A&ASS*, 136, 429 [3]
 Dent, W. R. F., Greaves, J. S., & Coulson, I. M. 2005, *MNRAS*, 359, 663 [3]
 Donehew, B., & Brittain, S. 2011, *AJ*, 141, 46 [3]
 Dupree, A. K., Brickhouse, N. S., Smith, G. H., & Strader, J. 2005, *ApJ*, 625, L131 [5.4]
 Edwards, S., Hartigan, P., Ghandour, L., & Andrulic, C. 1994, *AJ*, 103, 3 [6.2, 11]
 Edwards, S., Fischer, W., Hillenbrand, L., & Kwan, J. 2006, *ApJ*, 646, 319 [5.3, 6.4]
 Eisner, J. A., Lane, B. F., Hillenbrand, L. A., Akeson, R. L., & Sargent, A. I. 2004, *ApJ*, 613, 1049 [3]
 Eisner, J. A., Graham, J. R., Akeson, R. L., & Najita, J. 2009, *ApJ*, 692, 309 [3]
 Ellerbroek, L. E., et al. 2014, *A&A*, 563, A87 [6.4]
 Feigelson, E. D., & Babu, G. J. 2012, *Modern Statistical Methods for Astronomy* (New York, NY: CUP) [3, 5.4]
 Fekel, F. C. 2003, *PASP*, 115, 807 [3]
 Finkenzeller, U., & Jankovics, I. 1984, *A&ASS*, 57, 285 [3, 7]
 Finkenzeller, U., & Mundt, R. 1984, *A&ASS*, 55, 109 [1, 2, 3, 5.3]
 Fischer, W., Kwan, J., Edwards, S., & Hillenbrand, L. 2008, *ApJ*, 687, 1117 [6.2, 11, 6.2]
 Fuente, A., Martín-Pintado, J., Bachiller, R., Rodríguez-Franco, & Palla, F. 2002, *A&A*, 387, 977 [3]
 Fukagawa, M., Tamura, M., Itoh, Y., Hayashi, S. S., & Oasa, Y. 2003, *ApJ*, 590, L49 [3]
 Garcia Lopez, R., Natta, A., Testi, L., & Habart, E. 2006, *A&A*, 459, 837 [3]
 Grady, C. A., et al. 2004, *ApJ*, 608, 809 [6.4]
 Grady, C. A., et al. 2010, *ApJ*, 719, 1565 [1]
 Guilloteau, S., Dutrey, A., Piétu, V., & Boehler, Y. 2011, *A&A*, 529, A105 [3]
 Guilloteau, S., Di Folco, E., Dutrey, A., Simon, M., Grosso, N., & Piétu, V. 2013, *A&A*, 549, A92 [3]
 Halbedel, E. H. 1996, *PASP*, 108, 833 [3]
 Hamann, F., & Persson, S. E. 1992, *ApJSS*, 82, 285 [1, 5.3, 6.1]
 Hartigan, P., Edwards, S., & Ghandour, L. *ApJ*, 452, 736 [6.4]
 Hernández, J., Calvet, N., Briceño, C., Hartmann, L., & Berlind, P. 2004, *ApJ*, 127, 1682 [3]
 Hillenbrand, L. A., Strom, S. E., Vrba, F. J., & Keene, J. 1992, *ApJ*, 397, 613 [3, 5.1, 5.1]
 Johns-Krull, C. M. 2007, *ApJ*, 664, 975 [1]
 Juhász, A., et al. 2010, *ApJ*, 721, 431 [3]
 Königl, A. 1991, *ApJ*, 370, L39 [1]
 Kraus, S., et al. 2008, *A&A*, 489, 1157 [1]
 Kraus, S., et al. 2013, *ApJ*, 768, 80 [3]

- Lee, H. T., & Chen, W. P. 2009, ApJ, 694, 1423 [3]
- Liu, W. M., et al. 2007, ApJ, 658, 1164 [3]
- Liu, T., Zhang, H., Wu, Y., Sheng-Li, Q., & Miller, M. 2011, ApJ, 734, 22 [3]
- Malfait, K., Bogaert, E., & Waelkens, C. 1998, A&A, 331, 211 [3, 5.1]
- Manoj, P., Bhatt, H. C., Maheswar, G., & Muneer, S. 2006, ApJ, 653, 657 [3]
- Mariñas, N., Telesco, C. M., Fisher, R. S., & Packham, C., 2011, ApJ, 737, 57 [3]
- Matt, S., & Pudritz, R. E. 2005, ApJ, 632, L135 [6.4]
- McCarthy, J. K., Sandiford, Brendan, A., Boyd, D., & Booth, J. 1993, PASP, 105, 881 [2.1]
- Meeus, G., Waters, L. B. F. M., Bouwman, J., van den Ancker, M. E., Waelkens, C., & Malfait, K. 2001, A&A, 365, 476 [5.1]
- Mendigutía, I., et al. 2011, A&A, 529, A34 [1, 3]
- Mendigutía, I., et al. 2011, A&A, 535, A99 [3]
- Millan-Gabet, R., Schloerb, F. P., & Traub, W. A. 2001, ApJ, 546, 358 [3]
- Muzerolle, J., Calvet, N., & Hartmann, L. 2001, ApJ, 550, 944 [1]
- Muzerolle, J., D'Alessio, P., Calvet, N., & Hartmann, L. 2004, ApJ, 617 [1, 6.2]
- Natta, A., Testi, L., Neri, R., Shepherd, D. S., & Wilner, D. J. 2004, A&A, 416, 179 [3]
- Okamoto, Y. K., et al. 2009, ApJ, 706, 665 [3]
- Oudmaiher, R. D., van der Veen, W. E. C. J., Waters, L. B. F. M., Trams, N. R., Waelkens, C., & Engelsman, E. 1992, A&ASS, 96, 625 [3]
- Osorio, M., et al. 2014, ApJL, 791, L36 [3]
- Perrin, M. D., Duchêne, G., Kalas, P., & Graham, J. R. 2006, ApJ, 645, 1272 [3]
- Perrin, M. D., Vacca, W. D., & Graham, J. R. 2009, AJ, 137, 4468 [3]
- Ragland, S., et al. 2012, ApJ, 746, 126 [3]
- Reed, B. C. 2003, AJ, 125, 2531 [3]
- Reipurth, B., Pedrosa, A., & Lago, M. T. V. T. 1996, A&ASS, 120, 229 [5.3]
- Romanova, M. M., Ustyugova, G. V., Koldoba, A. V., & Lovelace, R. V. E. 2009, MNRAS, 399, 1802 [1]
- Sartori, M. J., Gregorio-Hetem, J., Rodrigues, C. V., Hetem Jr., A., & Batalha, C. 2010, AJ, 139, 27 [3]
- Scheegerer, A. A., Ratzka, T., Schuller, P. A., Wolf, S., Mosoni, L., & Leinert, Ch. 2013, A&A, 555, A103 [3]
- Schütz, O., Meeus, G., & Sterzik, M. F. 2005, A&A, 431, 165 [3]
- Shu, F. H., Lizano, S., Ruden, S. P., & Najita, J. 1988, ApJ, 328, L19 [6.4]
- Shu, F., et al. 1994, ApJ, 429, 781 [1]
- Tang, Y.-W., Guilloteau, S., Piétu, V., Dutrey, A., Ohashi, N., & Ho, P. T. P. 2012, A&A, 547, A84 [3]
- Thé, P. S., de Winter, D., & Pérez, M. R. 1994, A&ASS, 104,315 [2, 3]
- Thi, W.-F., et al. 2014, A&A, 561, A50 [3]
- Tull, R. G., MacQueen, P. J., Sneden, C., & Lambert, D. L. 1995, PASP, 107, 251 [2.1]
- Verhoeff, A. P., et al. 2012, A&A, 538, A101 [3]
- Vieira, S. L. A., et al. 2003, AJ, 126, 2971 [1, 2, 3, 5.3]
- Vink, J. S., Drew, J. E., Harries, T. J., & Oudmaiher, R. D. 2002, MNRAS, 337, 356 [3]
- Wade, G. A., Bagnulo, S., Drouin, D., Landstreet, J. D., & Monin, D. 2007, MNRAS, 376, 1145 [1]
- Wilson, E. B. 1927, *Journal of the American Statistical Association*, 22, 158 [5.2]

APPENDIX

OPTICAL LINE PROFILES

Below are the extracted profiles for a piece of the sample. The profiles for the entire sample will be available with the published version. The format of each figure is the same as Figure 3 and Figure 4.

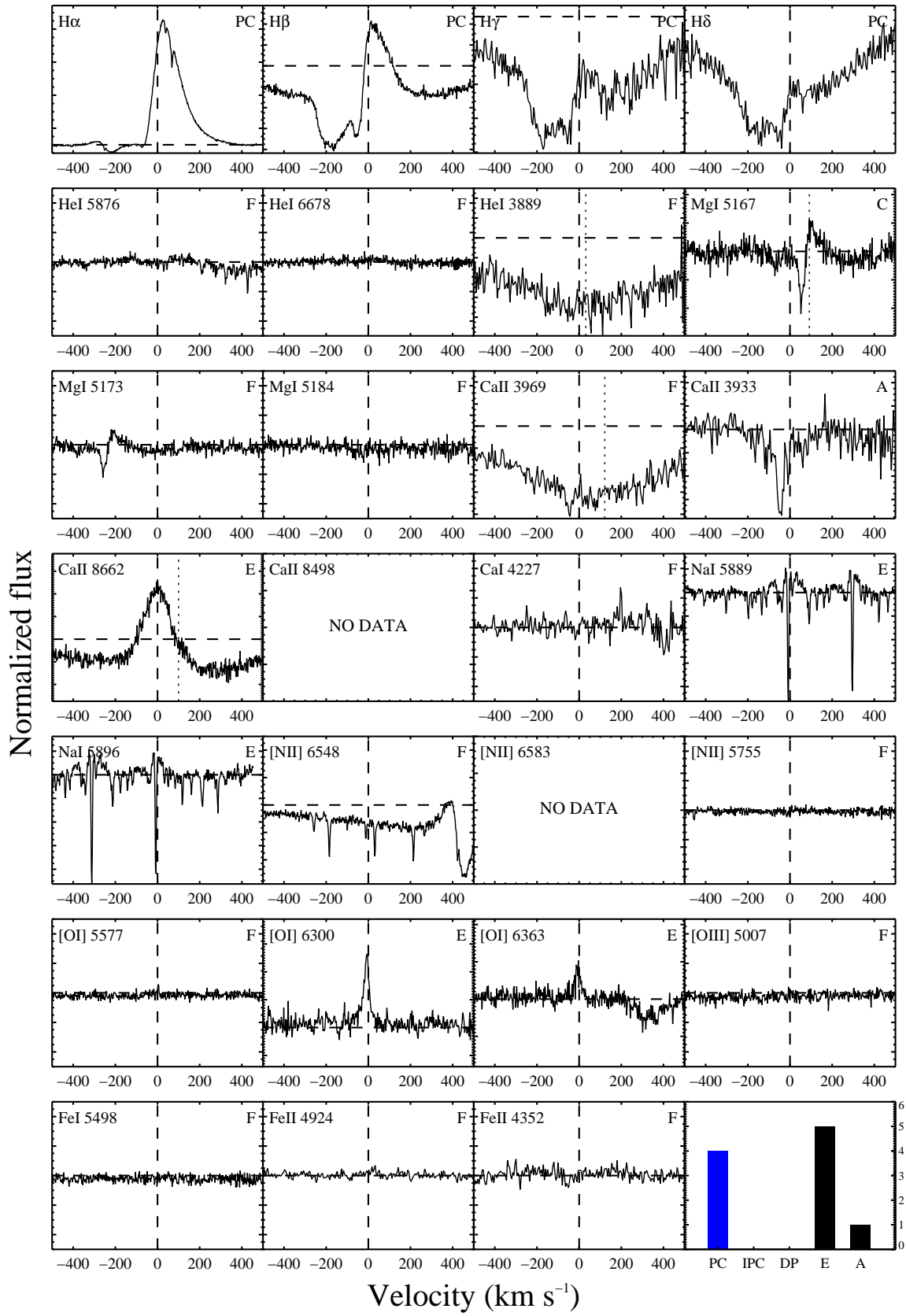


Figure 14. Extracted line profiles for AB Aur.

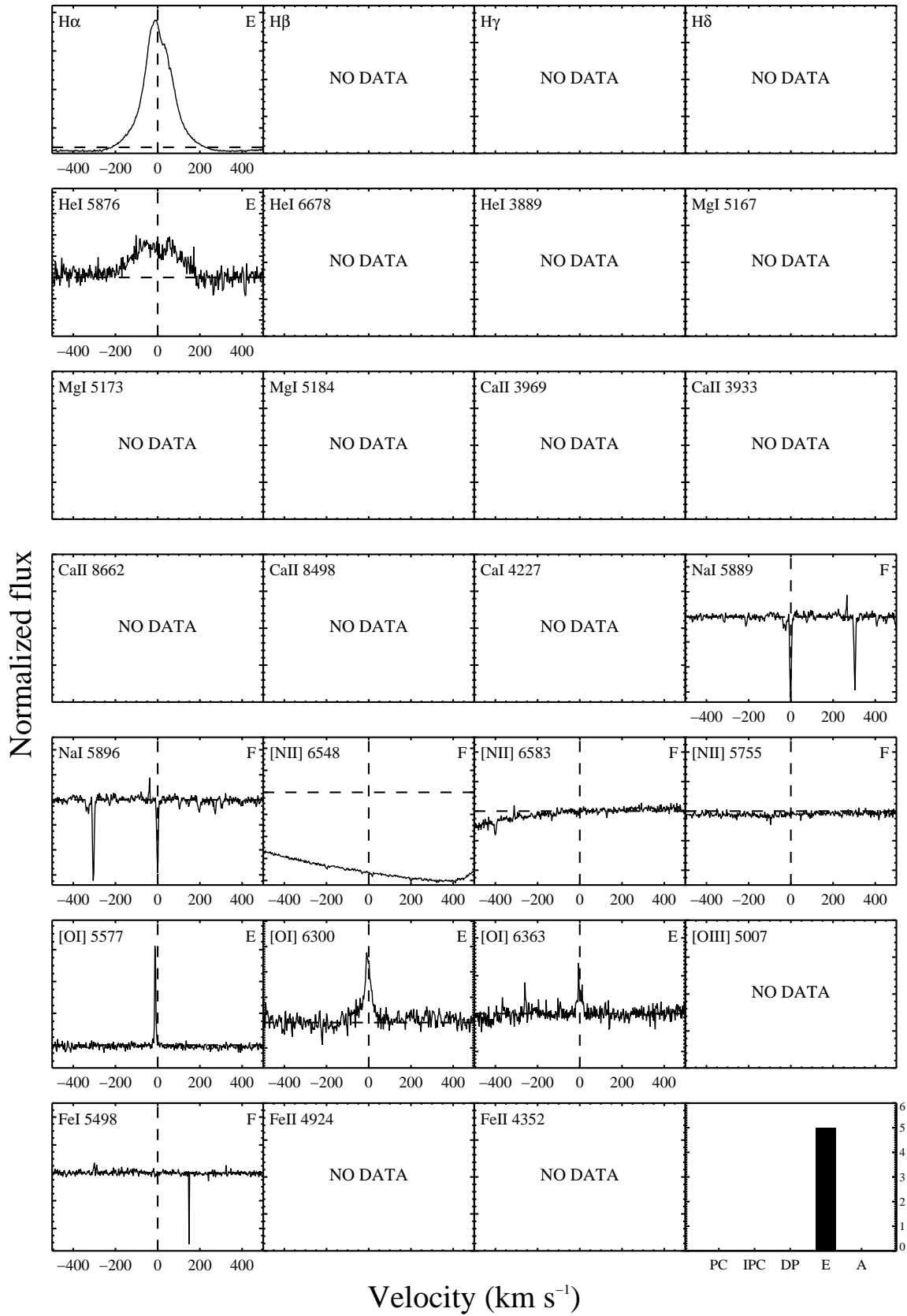


Figure 15. Extracted line profiles for AE Lep.

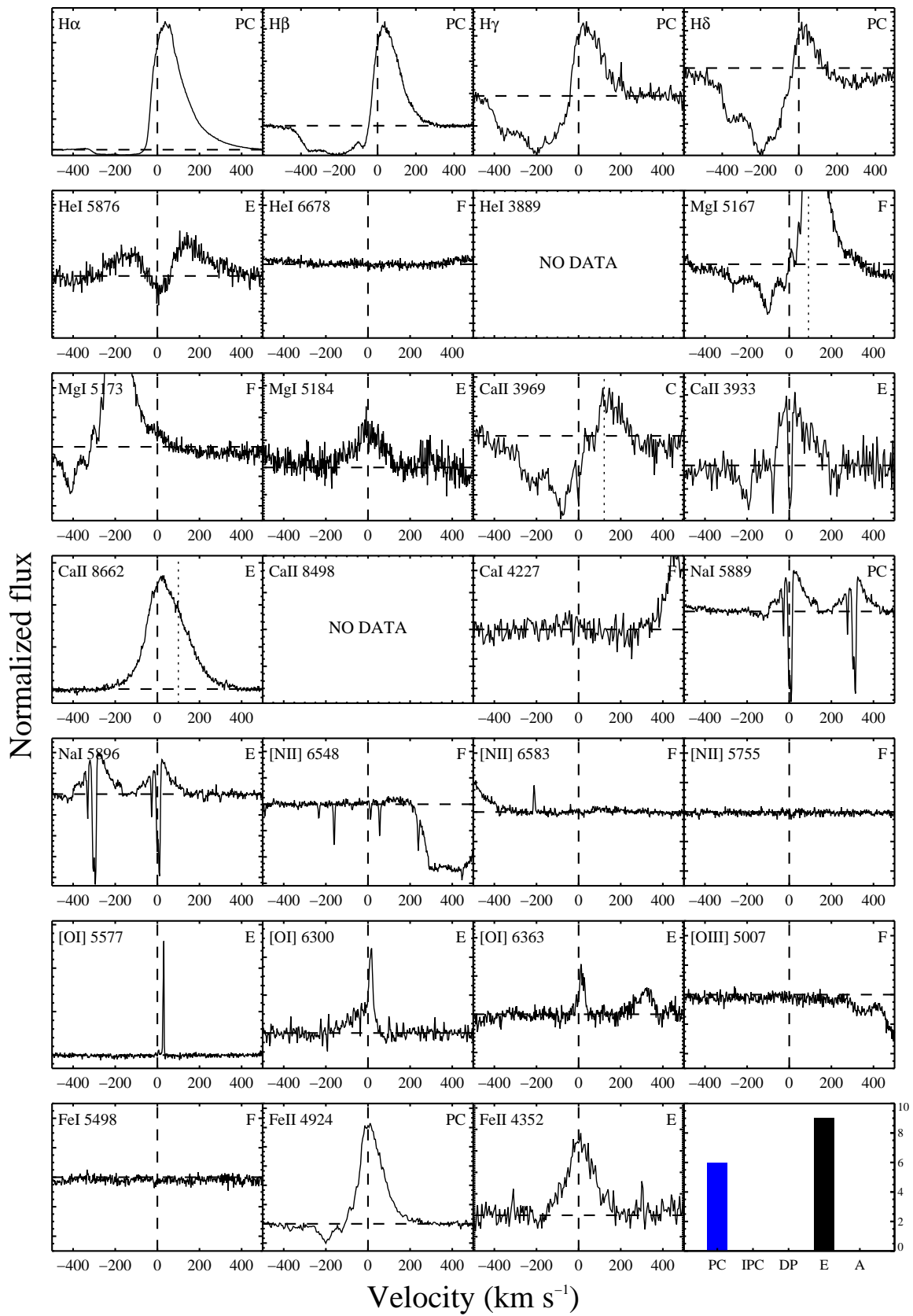


Figure 16. Extracted line profiles for BD+61 154.

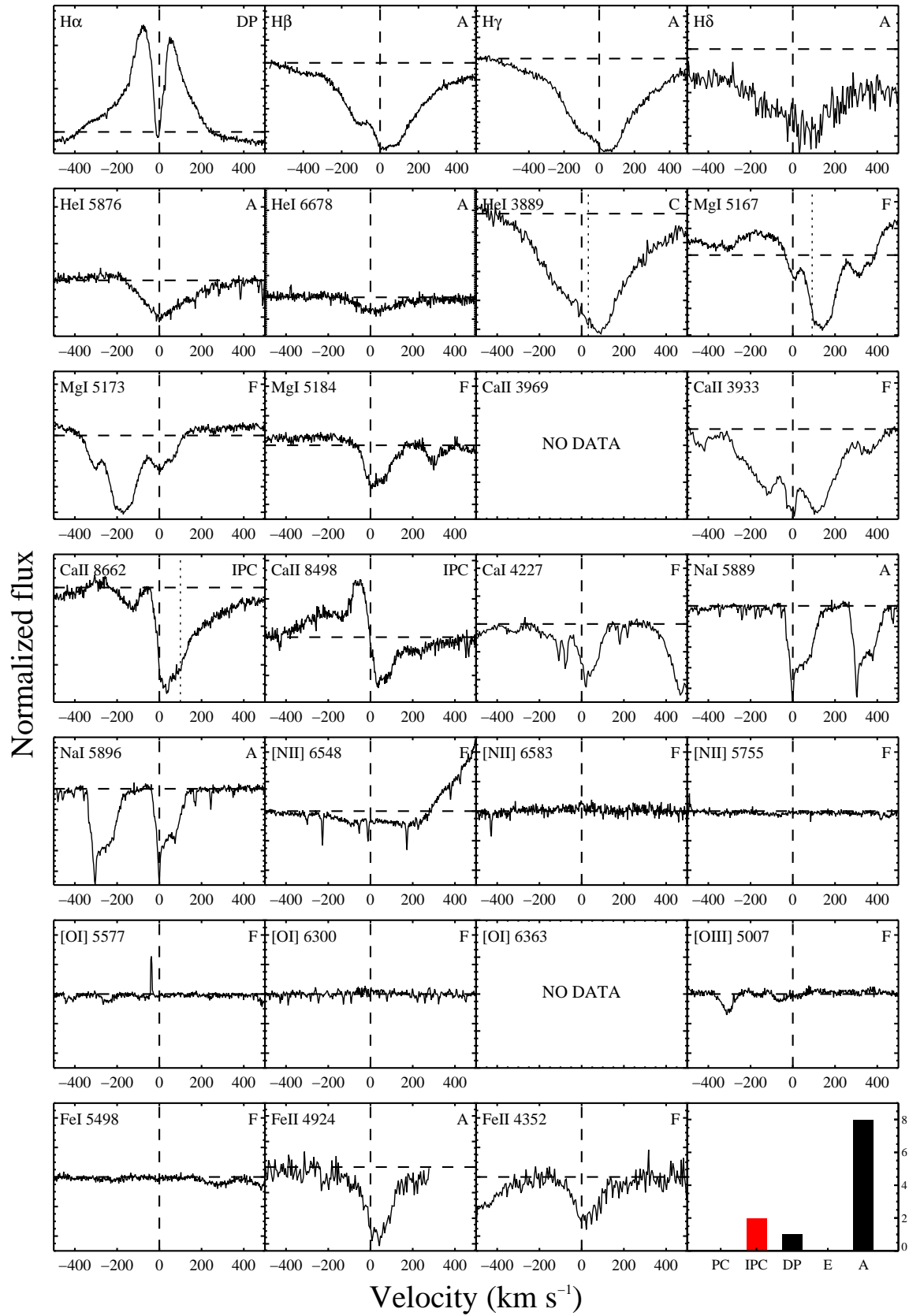


Figure 17. Extracted line profiles for BF Ori.

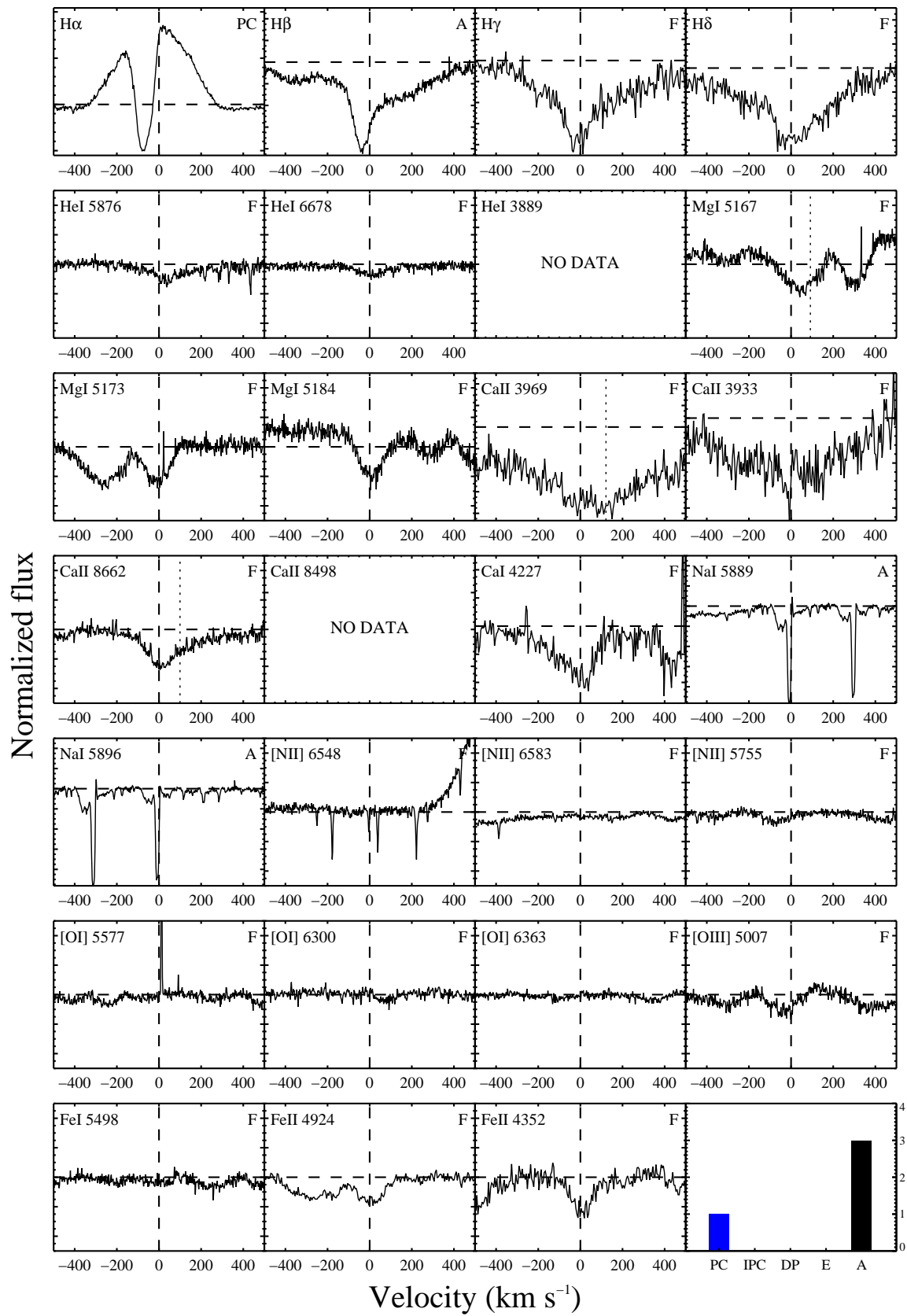


Figure 18. Extracted line profiles for BH Cep.

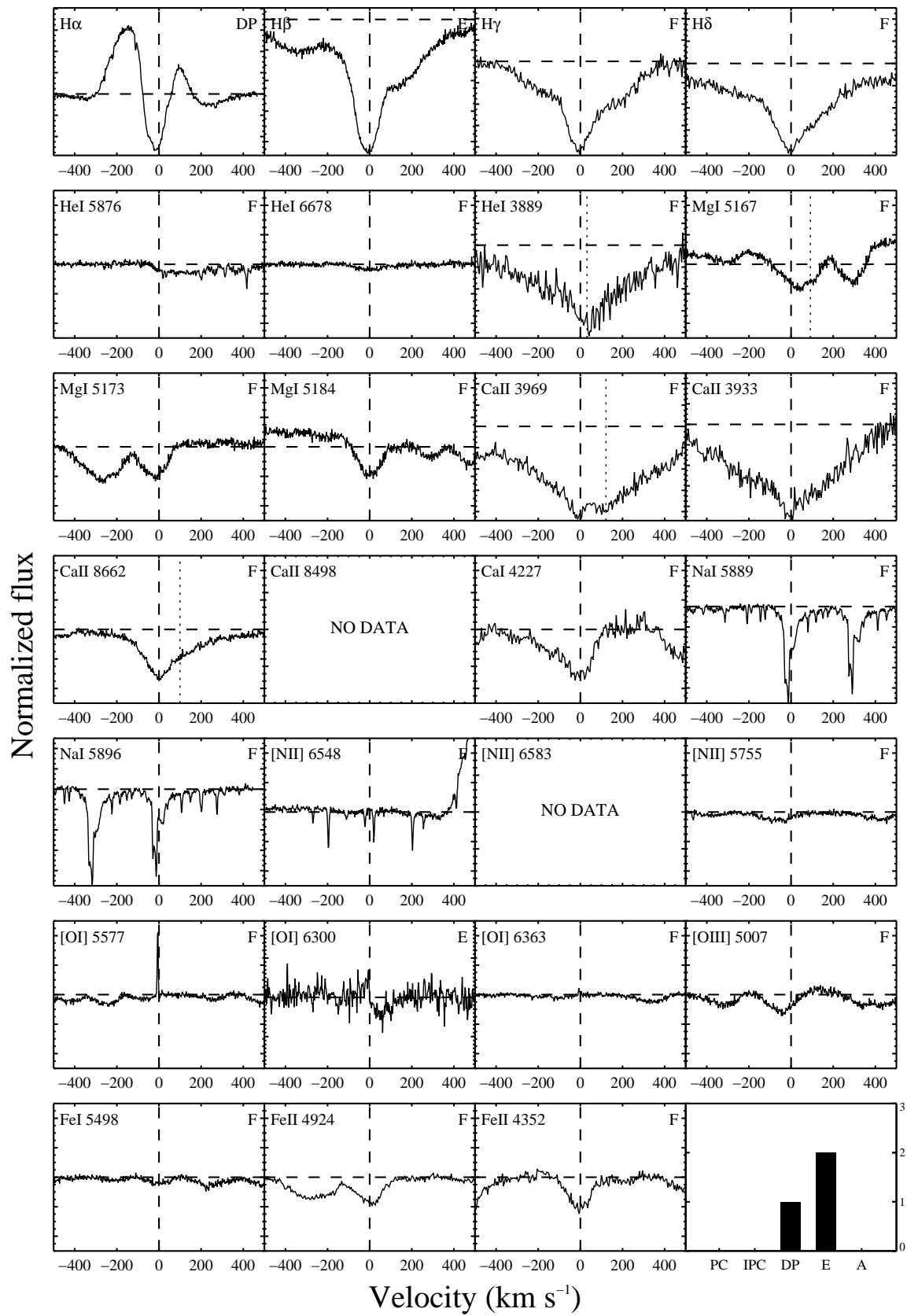


Figure 19. Extracted line profiles for CQ Tau.

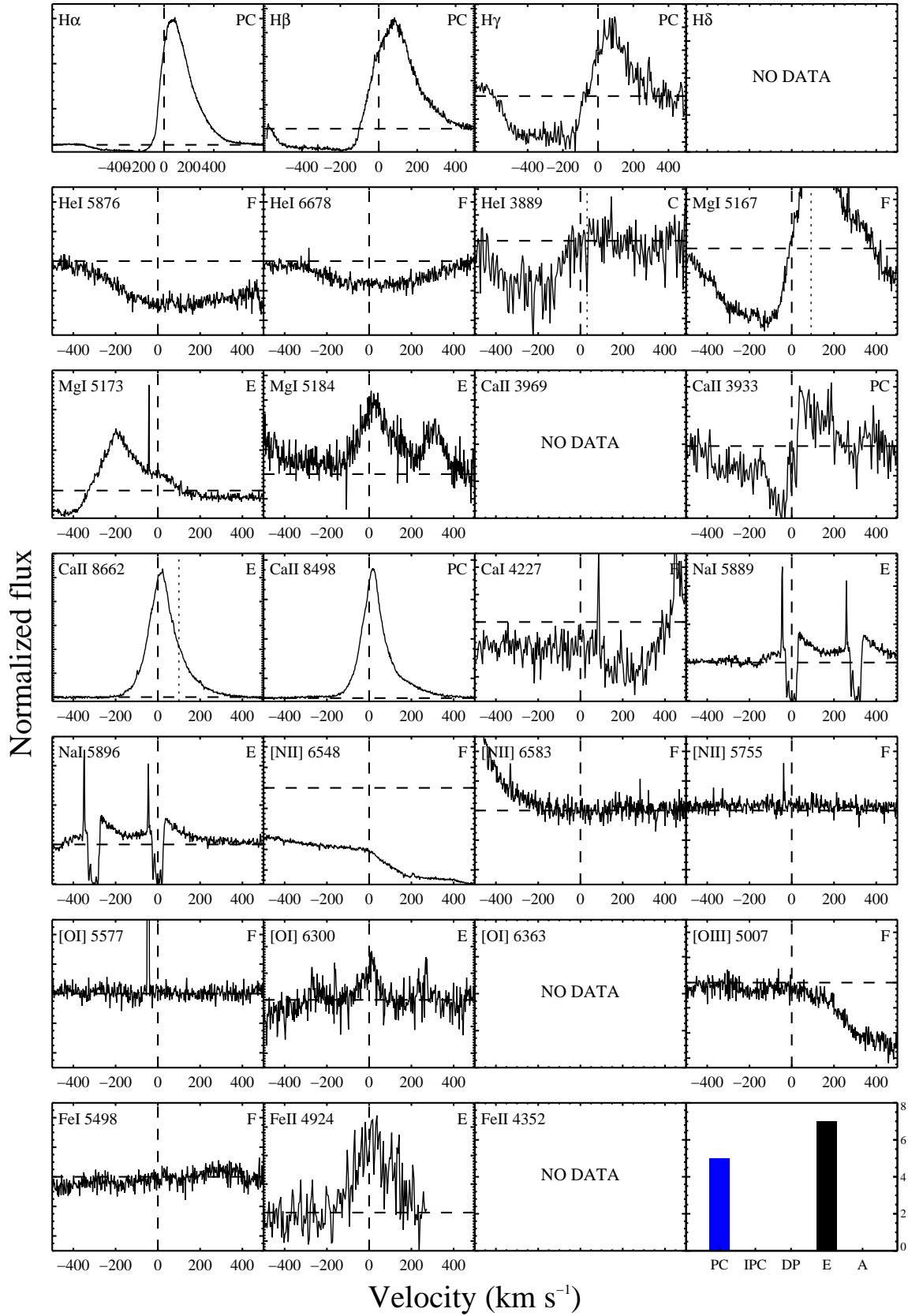


Figure 20. Extracted line profiles for DW CMA.

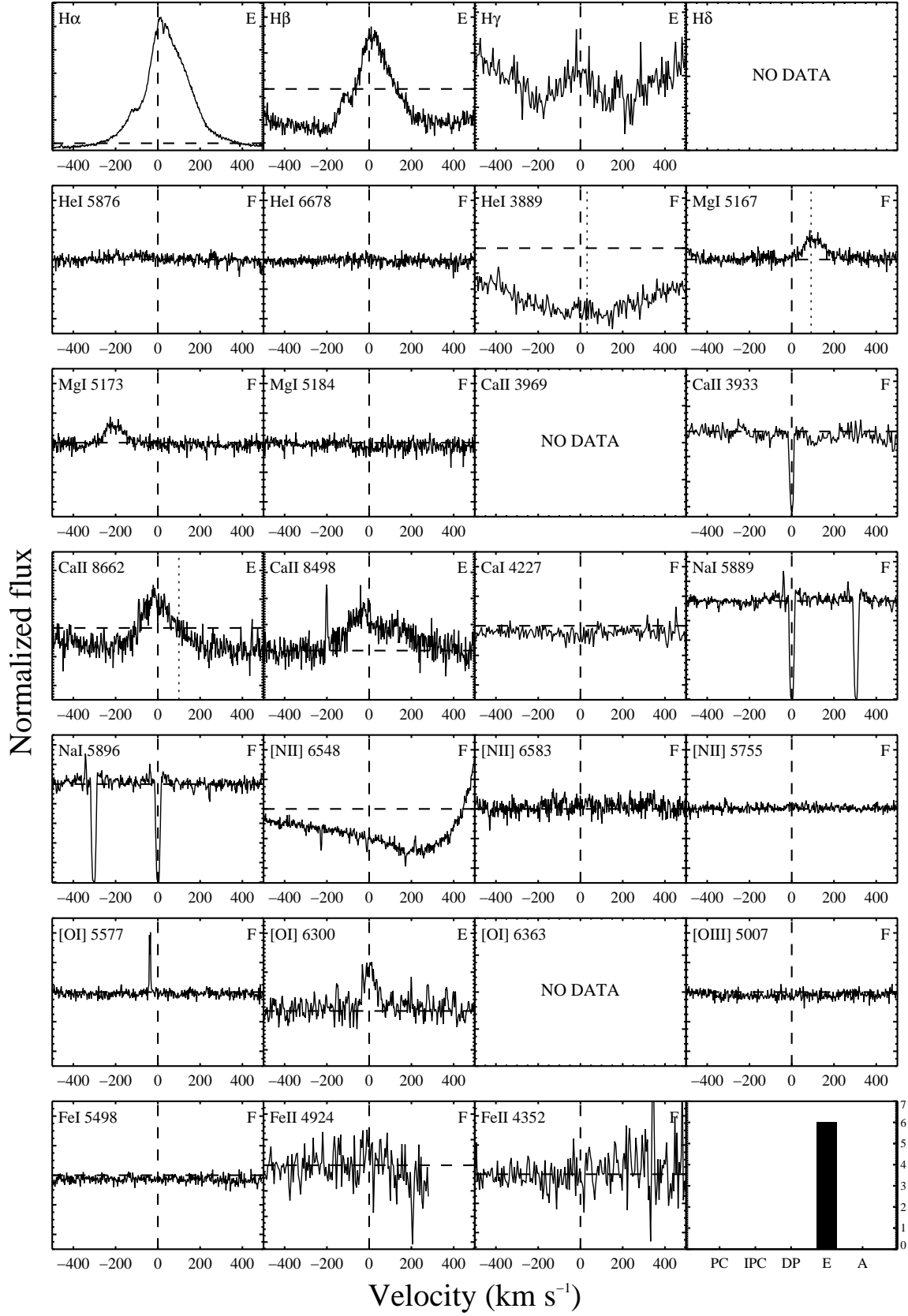


Figure 21. Extracted line profiles for GSC 04794-00827.

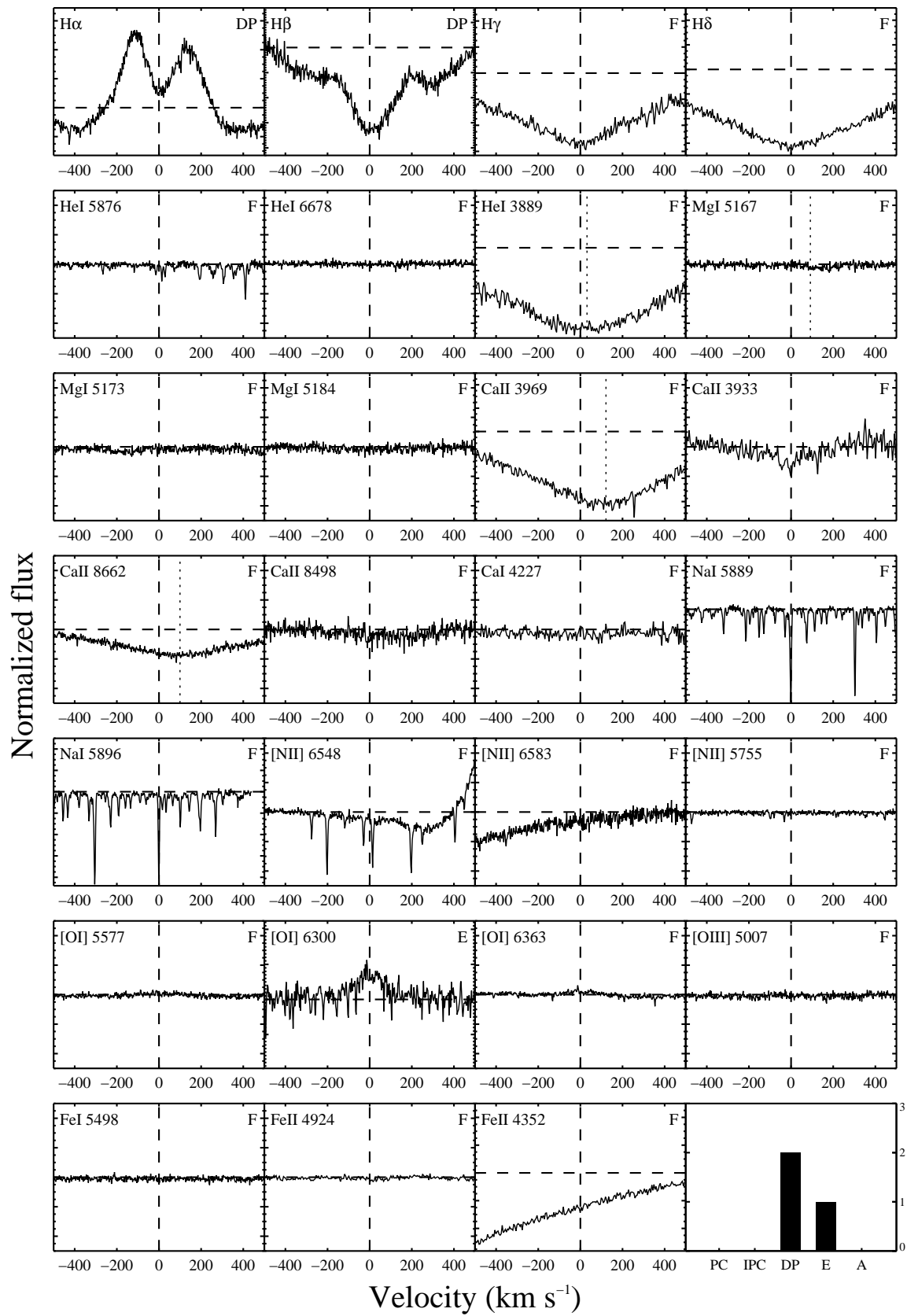


Figure 22. Extracted line profiles for HD 141569.

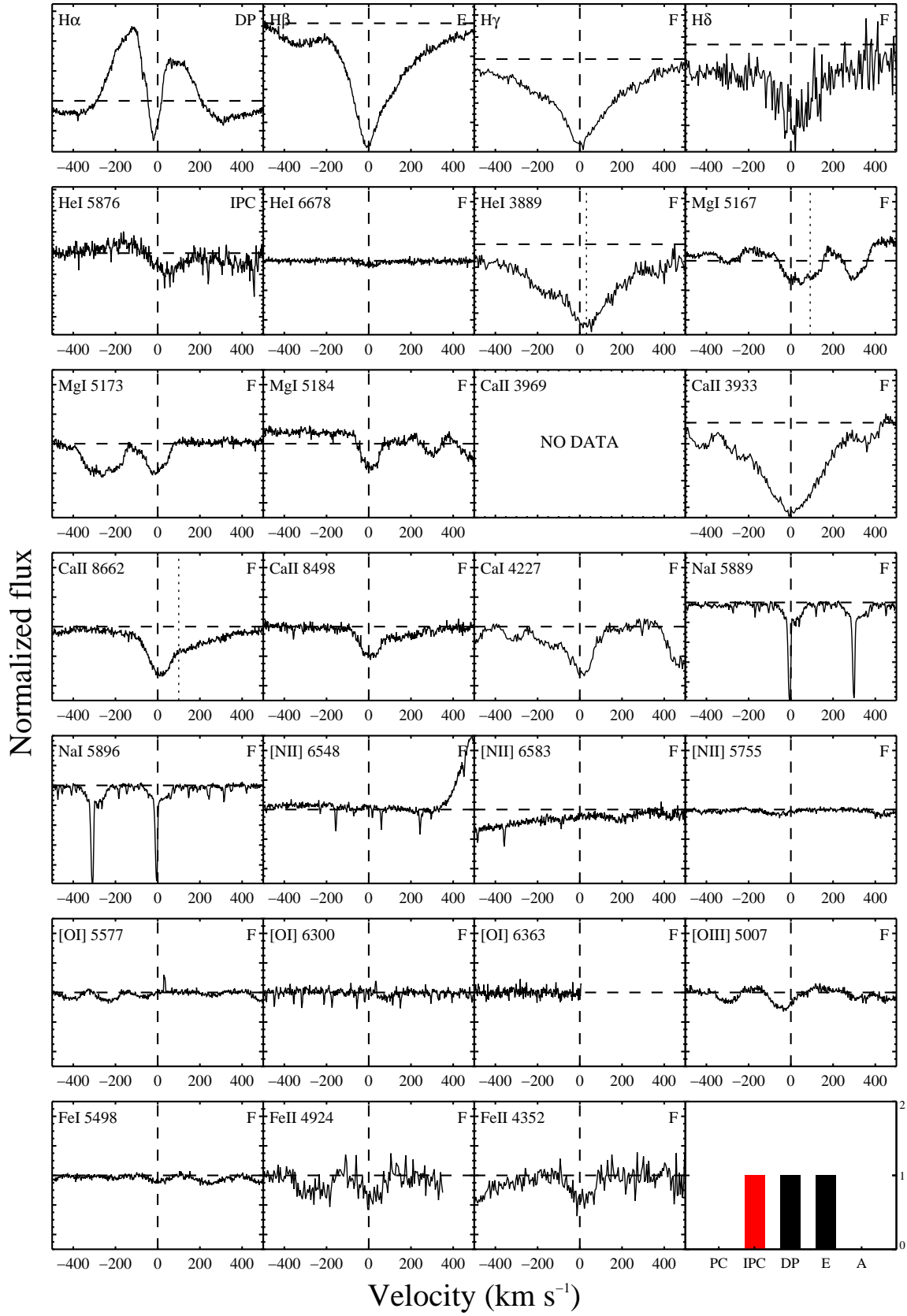


Figure 23. Extracted line profiles for HD 142666.

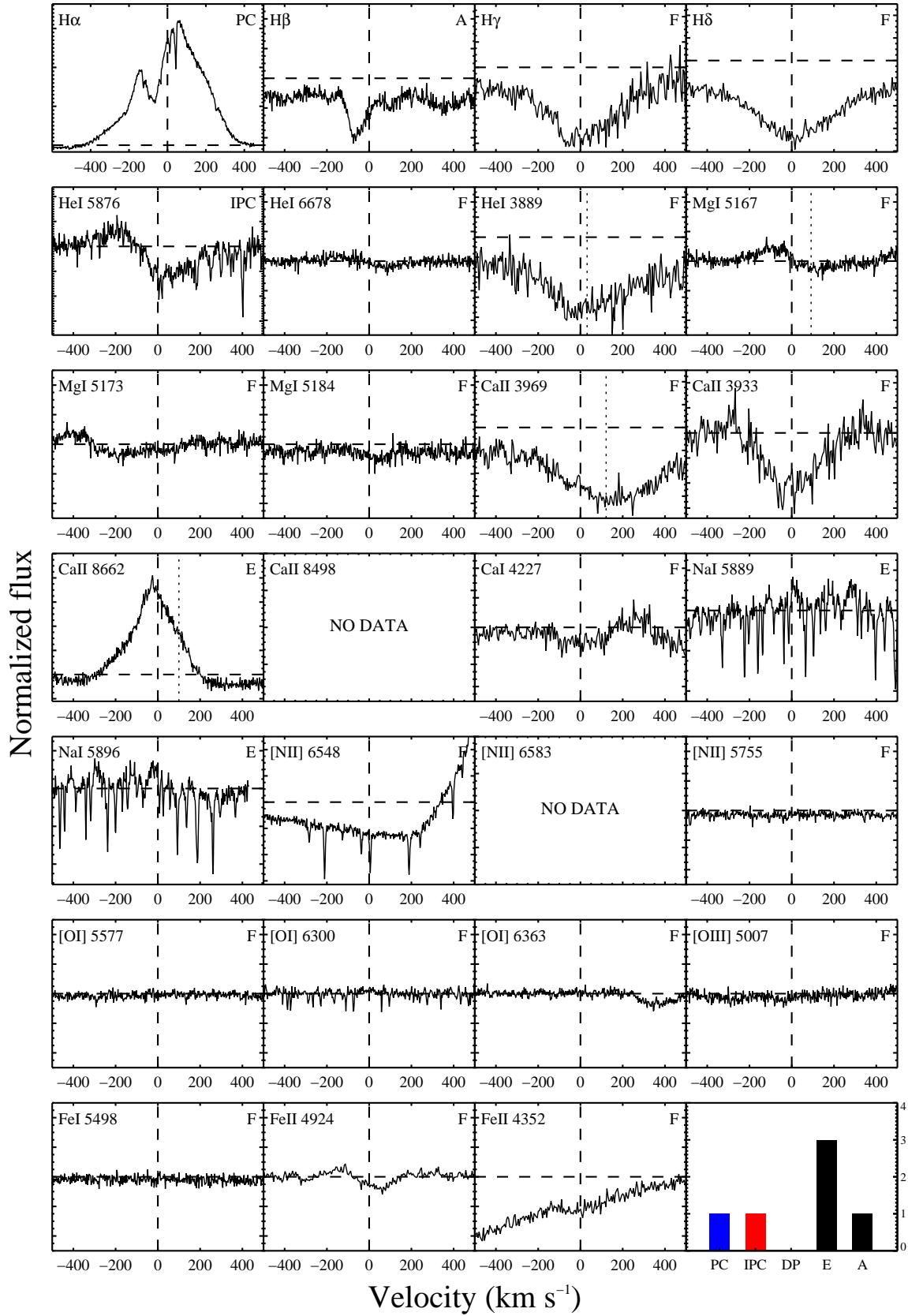


Figure 24. Extracted line profiles for HD 163296.

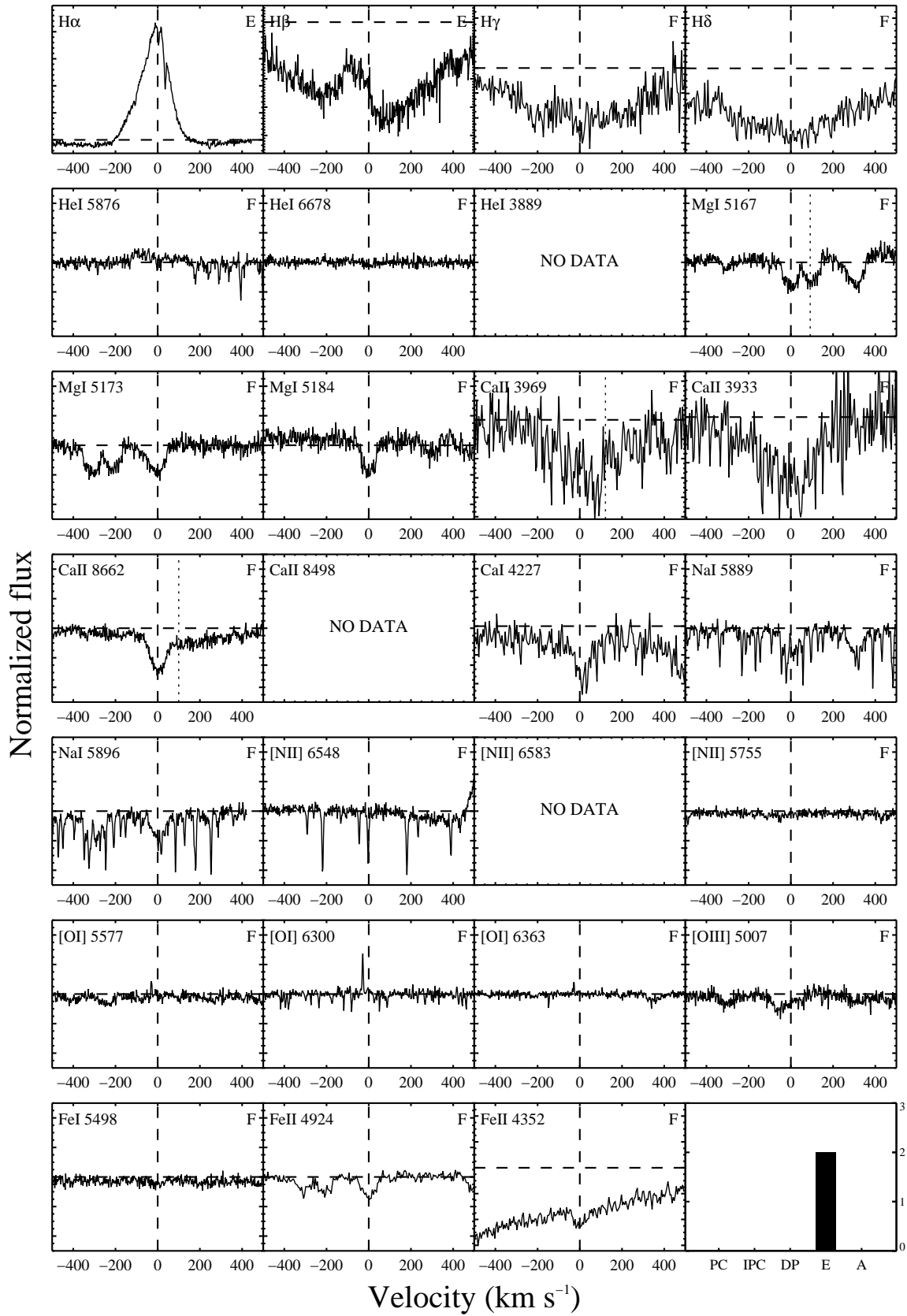


Figure 25. Extracted line profiles for HD 169142.

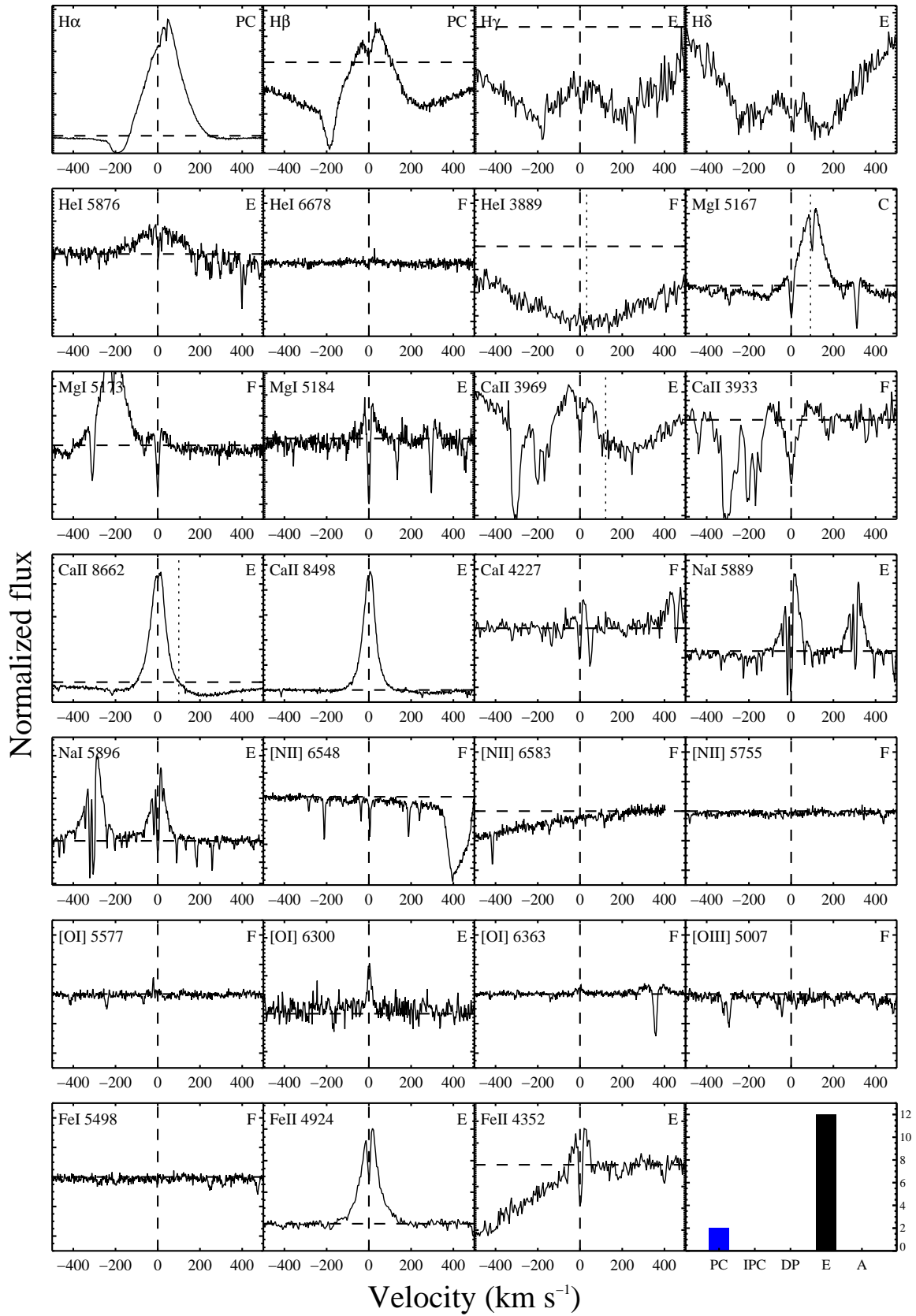


Figure 26. Extracted line profiles for HD 190073.

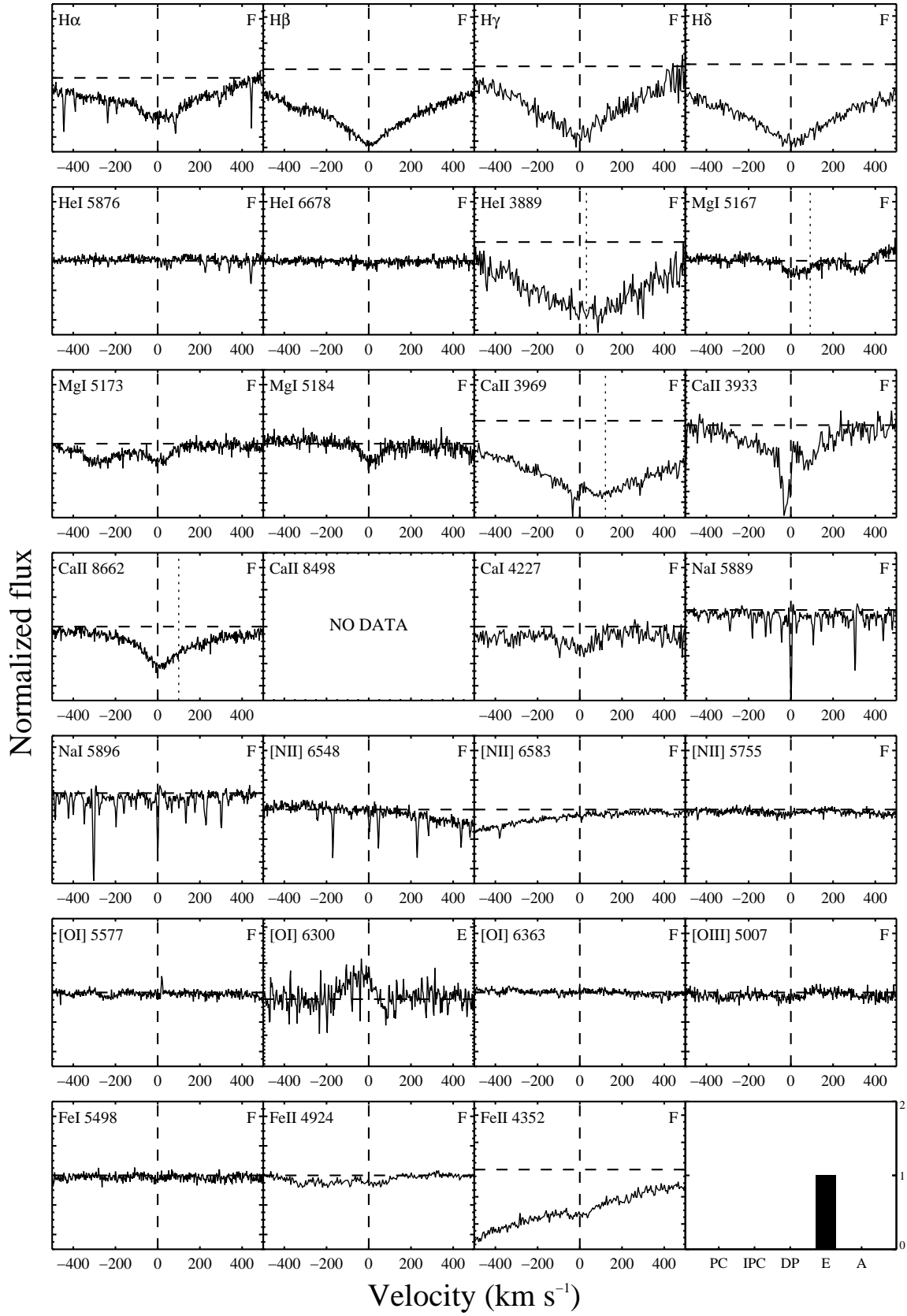


Figure 27. Extracted line profiles for HD 203024.

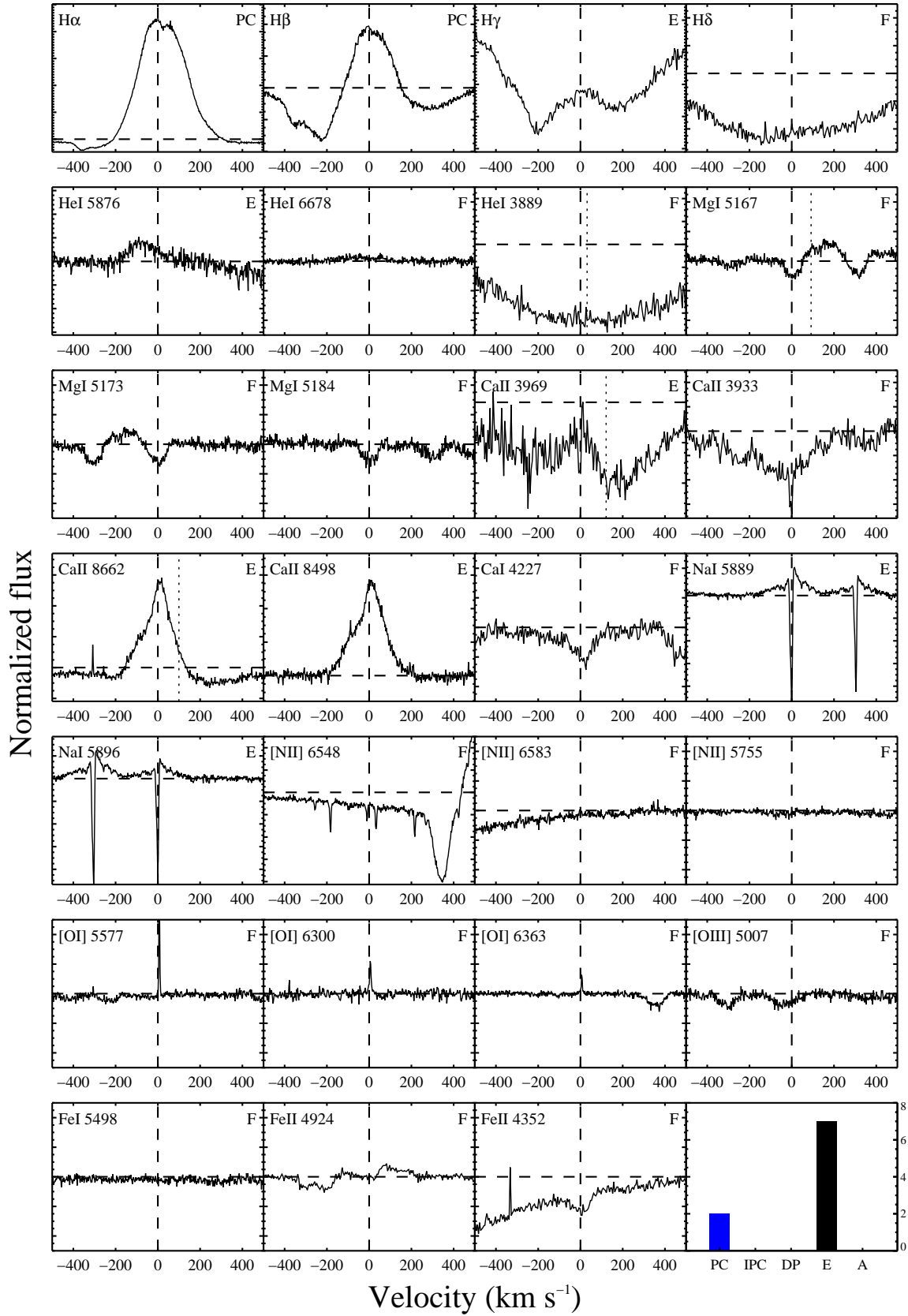


Figure 28. Extracted line profiles for HD 244314.

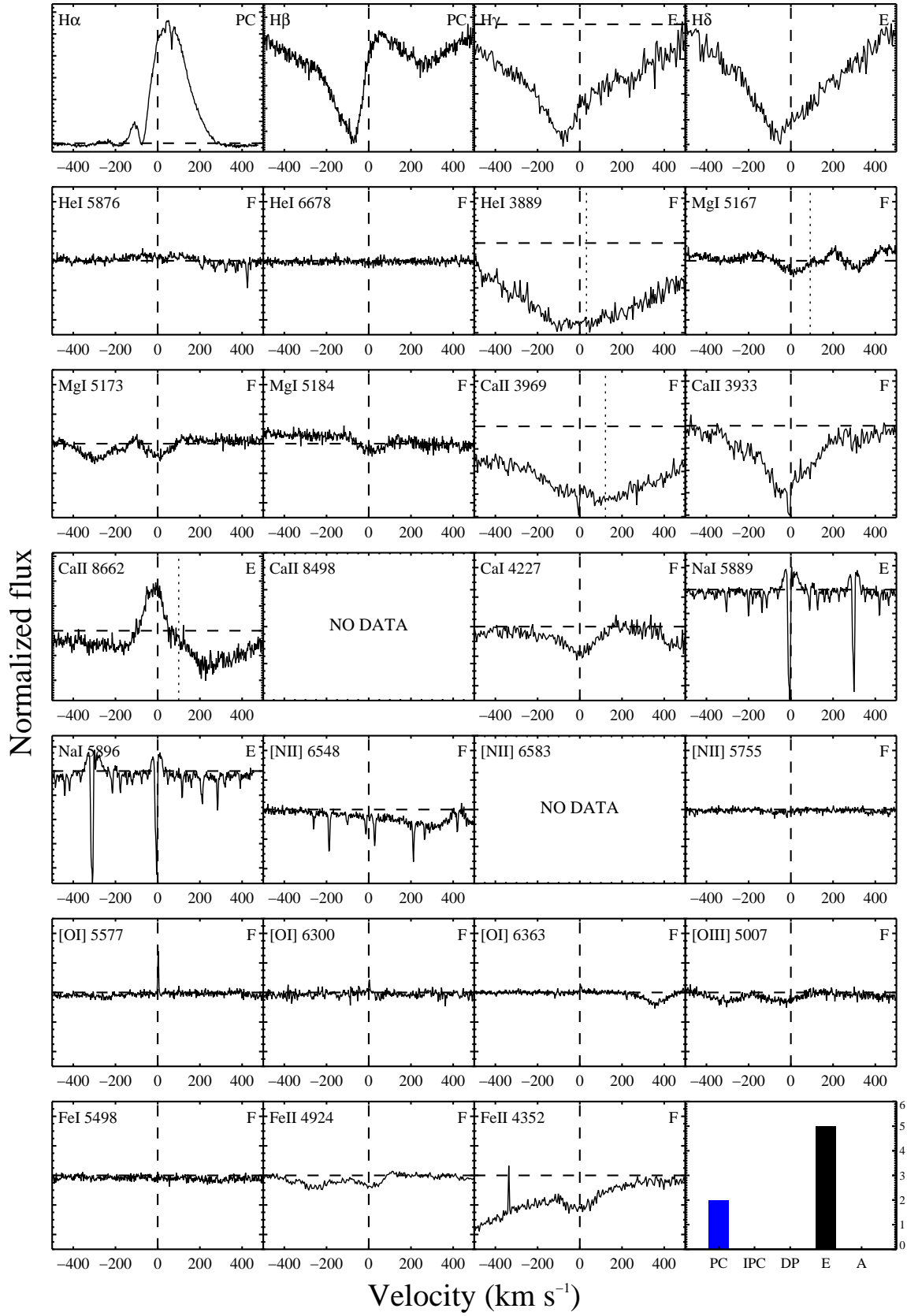


Figure 29. Extracted line profiles for HD 244604.

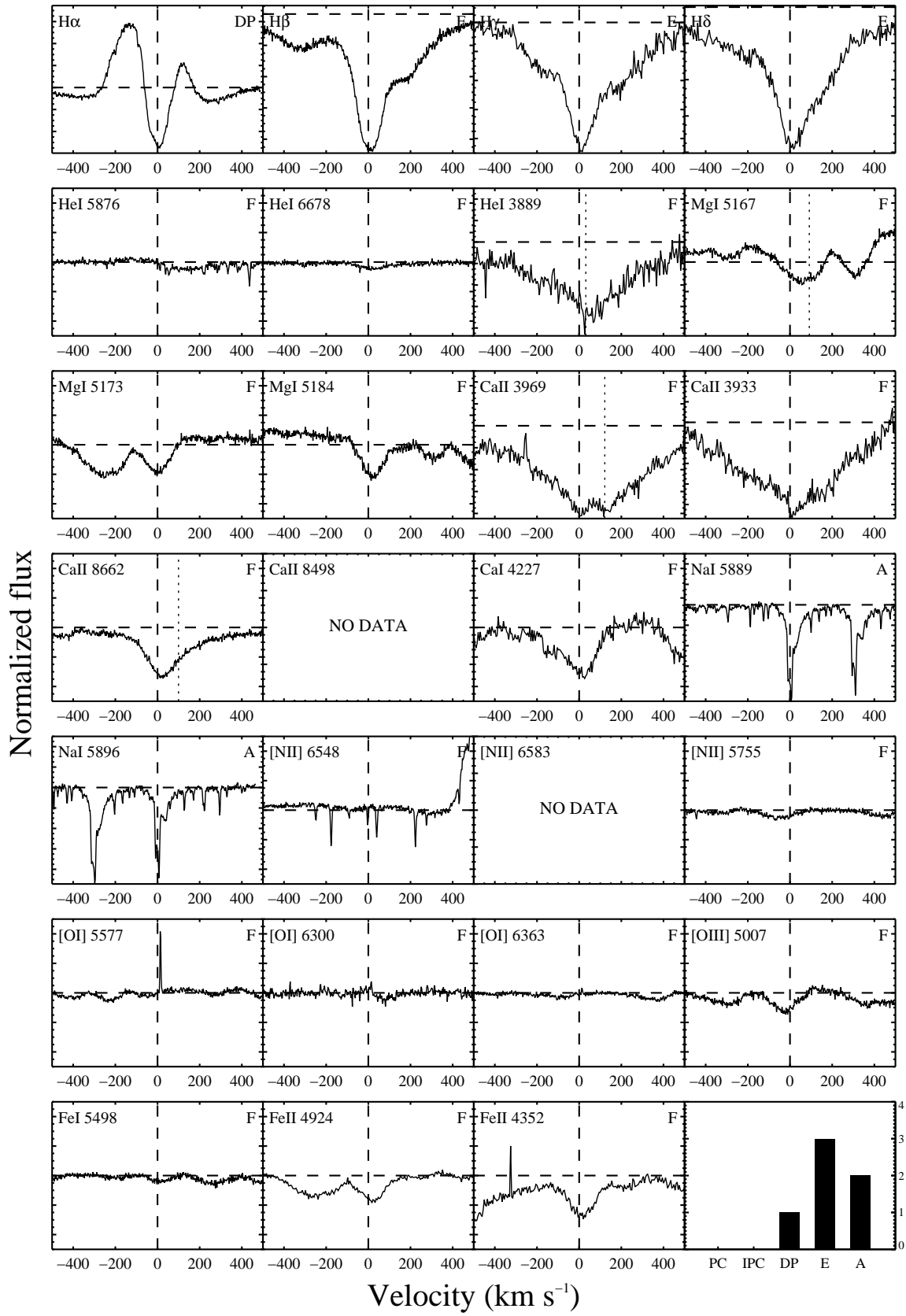


Figure 30. Extracted line profiles for HD 245185.

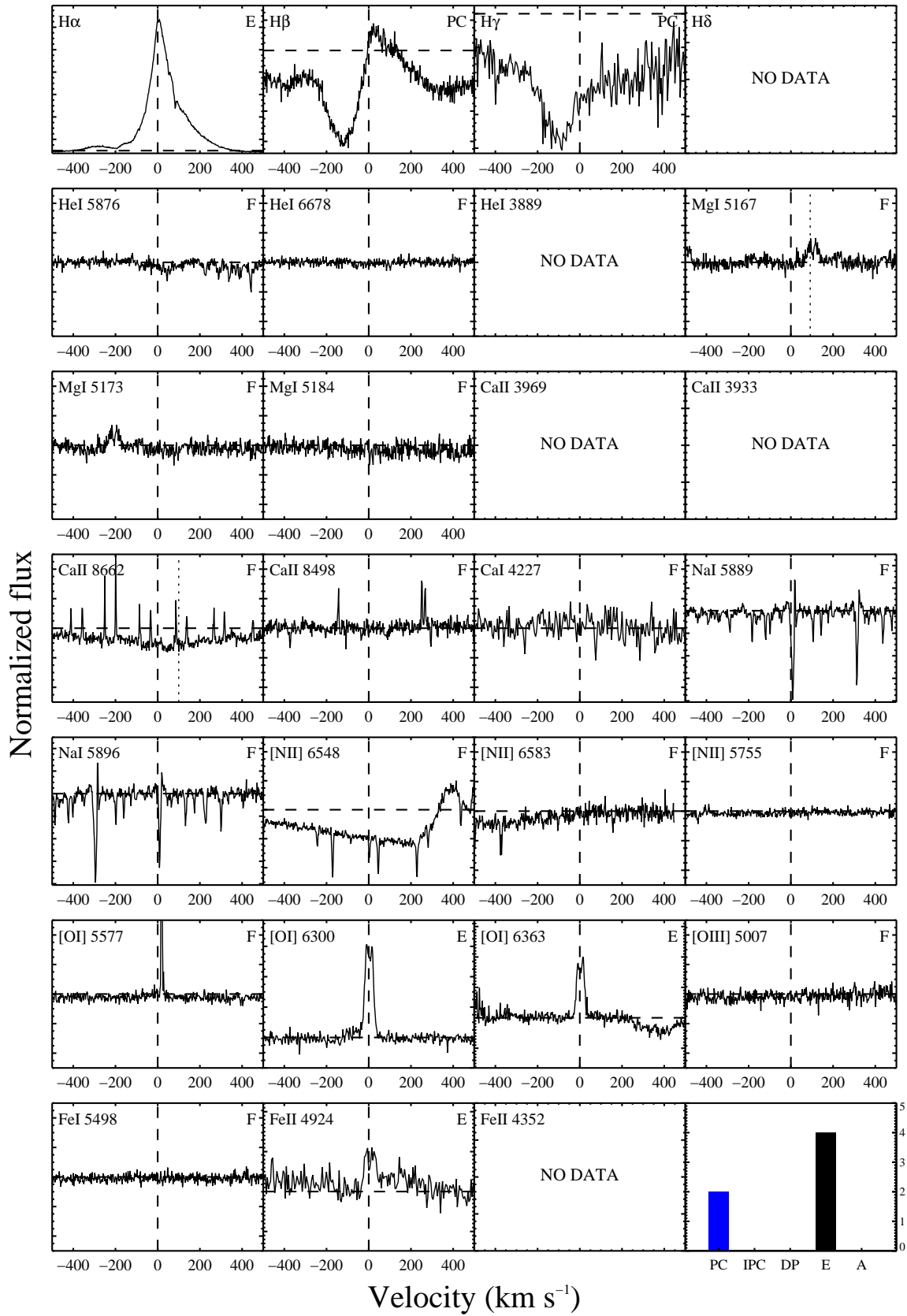


Figure 31. Extracted line profiles for HD 249879.